

AD-A246 943



2

MODELING OF CLOUD/RADIATION PROCESSES FOR LARGE-SCALE
CLOUDS AND TROPICAL ANVILS

K. N. Liou
J. L. Lee
S. C. Ou
Y. Takano

DTIC
ELECTE
MAR 05 1992
S D

AFOSR-TR- 92 0099

Center for Atmospheric and Remote Sounding Studies
Department of Meteorology
University of Utah
Salt Lake City, UT 84112

Interim Report
1 November 1990 - 31 October 1991

25 November 1991

This document has been approved
for public release and sale; its
distribution is unlimited.

92-05624



92 8 03 150

MODELING OF CLOUD/RADIATION PROCESSES FOR LARGE-SCALE
CLOUDS AND TROPICAL ANVILS

K. N. Liou
J. L. Lee
S. C. Ou
Y. Takano

Center for Atmospheric and Remote Sounding Studies
Department of Meteorology
University of Utah
Salt Lake City, UT 84112

Interim Report
1 November 1990 - 31 October 1991

25 November 1991

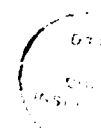
REPORT DOCUMENTATION PAGE

REPORT SECURITY CLASSIFICATION Unclassified		1b. RESTRICTIVE MARKINGS	
SECURITY CLASSIFICATION AUTHORITY		3. DISTRIBUTION/AVAILABILITY OF REPORT Approved for public release; distribution unlimited	
DECLASSIFICATION/DOWNGRADING SCHEDULE			
PERFORMING ORGANIZATION REPORT NUMBER(S)		5. MONITORING ORGANIZATION REPORT NUMBER(S)	
NAME OF PERFORMING ORGANIZATION enter for Atmospheric and remote Sounding Studies	6b. OFFICE SYMBOL (if applicable) CARSS	7a. NAME OF MONITORING ORGANIZATION Air Force Office of Scientific Research	
ADDRESS (City, State, and ZIP Code) Department of Meteorology University of Utah Salt Lake City, Utah 84112		7b. ADDRESS (City, State, and ZIP Code) Bolling Air Force Base Washington, D.C. 20332	
NAME OF FUNDING/SPONSORING ORGANIZATION AFOSR	8b. OFFICE SYMBOL (if applicable) NL	9. PROCUREMENT INSTRUMENT IDENTIFICATION NUMBER AFOSR-91-0039	
ADDRESS (City, State, and ZIP Code) Building 410 Bolling AFB DC 20332-6448		10. SOURCE OF FUNDING NUMBERS	
		PROGRAM ELEMENT NO. 61102F	PROJECT NO. 2310
		TASK NO. C3	WORK UNIT ACCESSION NO.
TITLE (Include Security Classification) Modeling of Cloud/Radiation Processes for Large-Scale Clouds and Tropical Anvils			
PERSONAL AUTHOR(S) K.N. Liou, J.L. Lee, S.C. Ou and Y. Takano			
1. TYPE OF REPORT Interim Annual	13b. TIME COVERED FROM 11/1/90 TO 10/31/91	14. DATE OF REPORT (Year, Month, Day) 1991, November, 25	15. PAGE COUNT
SUPPLEMENTARY NOTATION			
COSATI CODES		18. SUBJECT TERMS (Continue on reverse if necessary and identify by block number)	
FIELD	GROUP	SUB-GROUP	
		Cloud modeling, parameterization of microphysical processes, radiative transfer	
ABSTRACT (Continue on reverse if necessary and identify by block number) This interim report consists of three scientific papers:			
<p>a. Lee, J.L., K.N. Liou and S.C. Ou, 1991: A three-dimensional large-scale cloud model: Testing the role of radiative heating and ice phase processes. Submitted to <u>Tellus</u> for publication.</p> <p>b. Liou, K.N., J.L. Lee, S.C. Ou, Q. Fu and Y. Takano, 1991: Ice cloud microphysics, radiative transfer and large-scale cloud processes. <u>Meteorol. Atmos. Phys.</u>, 46, 41-50.</p> <p>c. Takano, Y. and K.N. Liou, 1991: Infrared polarization signature from cirrus clouds. <u>Applied Optics</u>, (in press).</p>			
DISTRIBUTION/AVAILABILITY OF ABSTRACT <input checked="" type="checkbox"/> UNCLASSIFIED/UNLIMITED <input type="checkbox"/> SAME AS RPT <input type="checkbox"/> DTIC USERS		21. ABSTRACT SECURITY CLASSIFICATION Unclassified	
NAME OF RESPONSIBLE INDIVIDUAL Lt. Col. James Stobie		22b. TELEPHONE (Include Area Code) 202-767-5021	22c. OFFICE SYMBOL AFOSR

A THREE-DIMENSIONAL LARGE-SCALE CLOUD MODEL:
 TESTING THE ROLE OF RADIATIVE HEATING AND ICE PHASE PROCESSES

J. L. Lee, K. N. Liou and S.C. Ou

Department of Meteorology/CARSS
 University of Utah
 Salt Lake City, Utah 84112



Accession For	
NTIS	CRA&I
DTIC	IAB
Unannounced	
Justification	
By	
Distribution	
Availability Codes	
Dist	Avail or for Special
A-1	

ABSTRACT

A time-dependent, three-dimensional, large-scale cloud model has been developed for the prediction of cloud cover, cloud liquid/ice water content (LWC/IWC), precipitation, specific humidity and temperature. Partial cloudiness is allowed to form when large-scale relative humidity is less than 100%. Both liquid and ice phases are included in the model. The liquid phase processes consist of evaporation, condensation, autoconversion and precipitation. The ice phase processes include heterogeneous nucleation to generate ice crystals, depositional growth to simulate Bergeron-Findeison's process, sublimation to deplete ice crystals, and gravitational settling of ice crystals. The radiative transfer parameterization program is based on a broadband method and involves the transfer of infrared and solar radiation in clear and cloudy regions. The broadband infrared emissivity, reflectivity, and transmissivity for cirrus clouds, as well as the broadband solar absorption, reflection, and transmission values for low, middle and high clouds are computed based on the cloud LWC and IWC interactively generated by the cloud model. Large amounts of satellite data, including cloud cover climatology derived from the U.S. Air Force three-dimensional nephanalysis (3DNEPH) and earth radiation budget (ERB), have been processed into formats appropriate for verification. The 96-hour model simulations of cloud cover, outgoing longwave radiation (OLR), and cloud LWC have been verified against data analyzed from 3DNEPH, ERB and the Nimbus-7 Scanning Multichannel Microwave Radiometer (SMMR) satellite observations, respectively. The predicted cloud IWC is compared to in situ observations as well as to results from other studies. The predicted cloud and radiation results compare well with those analyzed from satellite data. Numerical experiments are carried out with and without radiative heating and ice phase processes in the cloud formation

scheme. The inclusion of radiative heating produces a significant change in temperature, cloud cover and total cloud water content, while the inclusion of ice phase processes generates a substantial change only in total cloud water content. If the cloud LWC is sufficiently large to initiate effective Bergeron-Findeison's processes, the total cloud water content decreases, indicating that gravitational settling is an efficient mechanism in reducing the cloud IWC.

1. INTRODUCTION

Clouds regularly occupy about 50% of the sky. They are the most important regulators of the earth's radiation budget, i.e., the balance between incoming solar radiation and outgoing longwave radiation at the top of the atmosphere (TOA), by which the earth's climate is determined. On the one hand, clouds reflect a large portion of incoming solar radiation, producing a cooling effect referred to as the solar albedo effect. On the other, they trap the outgoing longwave radiation emitted from the earth, resulting in a warming effect referred to as the IR greenhouse effect. Since the greenhouse and albedo effects are different in sign as well as magnitude, the existence of clouds may have a profound impact upon the sensitivity of climate to external perturbations, such as the increase of atmospheric carbon dioxide. In particular, cirrus clouds, which regularly cover about 20% of the globe, are optically thin and nonblack. The outcome of the greenhouse-versus-albedo effects is intrinsically modified by the radiative effects of nonblack cirrus (Liou, 1986).

Recognizing the importance of clouds in weather and climate processes, numerous modeling efforts have been carried out to understand the relative significance of solar albedo and IR greenhouse effects involving clouds. In early models, the formation of clouds was very crude and lacked physical foundation. An arbitrary fractional amount of cloud was assigned to a given layer where large-scale condensation occurs. All the excessive water vapor was condensed and immediately precipitated onto the ground. As a result, there was no cloud water or cloud ice remaining in the clouds. These two elements are necessary for the calculation of cloud radiative effects. In climatic perturbation studies, Wetherald and Manabe (1988) assigned a cloud amount of 80% to condensation and found that cloud feedback processes enhance the sensitivity

of the model climate to an increase in atmospheric carbon dioxide. This conclusion is in agreement with that drawn by Hansen et al. (1983). The features of cloud cover change obtained in these studies, as well as in that of Washington and Meehl (1984), are qualitatively similar.

Efforts have also been focused on improving the specification of the radiative properties of clouds and cloud parameterization schemes in GCMs to demonstrate the importance of cloud-radiation interaction to the simulation of atmospheric circulation. Ramanathan et al. (1983) demonstrated that refinement in radiative properties of non-black high cirrus emissivity significantly improves the model simulation of atmospheric temperatures as well as that of zonal mean winds. Slingo and Slingo (1988) reached the same conclusion in their study of cloud longwave radiative forcing. Using a GCM designed for medium range weather prediction, Liou and Zheng (1984) illustrated the importance of cloud and radiative processes to the maintenance of the Hadley circulation.

In order to incorporate interactive cloud and radiation processes in models, cloud liquid water content (LWC) and ice water content (IWC) are required for radiation calculations. The models must be able to generate LWC/IWC. This is the so-called prognostic method, which requires the additional prognostic equation(s) for the prediction of LWC/IWC. Sundqvist (1978) made the first attempt to develop a physically based prognostic large-scale cloud scheme for use in a GCM. In his approach, the cloud LWC is a prognostic variable determined by various source and sink terms which are parameterized in terms of associated bulk quantities. Also partial cloudiness is allowed to exist when the large-scale relative humidity is less than 100%. Sundqvist (1981) incorporated the proposed cloud scheme into the European Center for Medium Range Weather Forecasts (ECMWF) GCM and carried out a 5-day integration. The forecast and cloud amounts were

compared with satellite photographs, which showed that the cloud patterns are reasonably well-simulated; the predicted cloud LWC is within the observational range. However, these studies did not include radiative effects and ice phase processes. The importance of including a more realistic and physically based parameterization for cloud parameters in GCMs has recently been articulated by Sundqvist (1988).

Mitchell et al. (1989) conducted a study of cloud feedback in the UK Meteorological Office GCM. A cloud liquid water budget equation was included in the model. However, ice clouds were not generated from the budget equation. Water cloud radiative properties are interactive in the model based on the schemes developed by Liou and Wittman (1979) for solar radiation and Stephens (1978) for IR radiation. Roeckner (1988) also included a water budget equation in the University of Hamburg GCM to undertake a study of the feedback processes involving clouds due to external radiative forcing. Smith (1990) incorporated a prognostic cloud water budget equation in a GCM and compared the simulated cloud and radiation fields with satellite observations.

Interactive cloud formation in a model setting would require a detailed consideration of the sources and sinks of water and ice particles. The inclusion of separate empirical equations for cloud LWC (e.g., Xu and Krueger, 1991), IWC (e.g., Heymsfield and Donner, 1990) and precipitation in the GCM diagnostic approach would appear to be extremely difficult and inconsistent with respect to the model physics. In order to understand the role of radiative heating and ice phase processes in the formation of large-scale clouds, we have developed a global stratiform cloud model that includes prognostic cloud LWC, IWC and precipitation equations as well as an interactive radiative transfer program. The wind fields required for the simulation are determined from a GCM. In

Section 2, we describe a large-scale cloud model and an interactive radiation program. Section 3 contains bulk parameterizations of various sources and sinks for the cloud microphysical processes simulated in the model. Section 4 presents comparisons of model predictions and verification data, including a description of model input and verification data. Results on the numerical experiments on atmospheric radiation and ice phase processes are shown in Section 5. Finally, conclusions are given in Section 6.

2. MODEL DESCRIPTION

a. Governing Equations

We have developed a time-dependent, three-dimensional cloud-moisture model for the prediction of water vapor, cloud LWC, cloud IWC, precipitation and temperature. The first four variables are governed by the law of mass conservation. The latent heat exchanges during the phase transitions of water substances are determined by the first law of thermodynamics through the temperature field. The governing equations may be written as follows:

$$\begin{aligned} \frac{\partial}{\partial t}(\bar{\rho}\bar{T}) + \frac{1}{a\cos\phi} \left[\frac{\partial}{\partial \lambda}(\bar{\rho}\bar{T}\bar{u}) + \frac{\partial}{\partial \phi}(\bar{\rho}\bar{T}\bar{v}\cos\phi) \right] + \frac{\partial}{\partial z}(\bar{\rho}\bar{T}\bar{w}) + \bar{\rho}\Gamma_d\bar{w} \\ = \bar{\rho}(\bar{Q}_c + \bar{Q}_a) - \frac{L_c}{C_p}\bar{E}_r + \frac{L_f}{C_p}\bar{S}_{BF} - \frac{L_d}{C_p}\bar{S}_s + F_H^I + F_V^I, \end{aligned} \quad (2.1)$$

$$\begin{aligned} \frac{\partial}{\partial t}(\bar{\rho}\bar{q}_v) + \frac{1}{a\cos\phi} \left[\frac{\partial}{\partial \lambda}(\bar{\rho}\bar{q}_v\bar{u}) + \frac{\partial}{\partial \phi}(\bar{\rho}\bar{q}_v\bar{v}\cos\phi) \right] + \frac{\partial}{\partial z}(\bar{\rho}\bar{q}_v\bar{w}) \\ = -\frac{C_p}{L_c}\bar{\rho}\bar{Q}_c + \bar{\rho}\bar{E}_r + \bar{S}_s + F_H^{qv} + F_V^{qv}, \end{aligned} \quad (2.2)$$

$$\begin{aligned} \frac{\partial}{\partial t}(\bar{\rho}\bar{q}_i) + \frac{1}{a\cos\phi} \left[\frac{\partial}{\partial \lambda}(\bar{\rho}\bar{q}_i\bar{u}) + \frac{\partial}{\partial \phi}(\bar{\rho}\bar{q}_i\bar{v}\cos\phi) \right] + \frac{\partial}{\partial z}[\bar{\rho}\bar{q}_i(\bar{w} - \bar{w}_i)] \\ = \frac{C_p}{L_c}\bar{\rho}\bar{Q}_c - \bar{\rho}\bar{P} - \bar{S}_{BF} + F_H^{qi} + F_V^{qi}, \end{aligned} \quad (2.3)$$

$$\begin{aligned} \frac{\partial}{\partial t}(\bar{\rho} \bar{q}_i) + \frac{1}{a \cos \phi} \left[\frac{\partial}{\partial \lambda}(\bar{\rho} \bar{q}_i \bar{u}) + \frac{\partial}{\partial \phi}(\bar{\rho} \bar{q}_i \bar{v} \cos \phi) \right] + \frac{\partial}{\partial z}[\bar{\rho} \bar{q}_i(\bar{w} - \bar{V}_T)] \\ = \frac{C_p}{L_d} \bar{\rho} \bar{Q}_i + \bar{S}_{BF} - \bar{S}_s + F_H^{qi} + F_V^{qi} , \end{aligned} \quad (2.4)$$

$$-\frac{\partial}{\partial z}(\bar{P}) = \bar{\rho} \bar{P} - \bar{\rho} \bar{E}_r . \quad (2.5)$$

In these equations, an overbar denotes the average of a variable over a grid space. The variables \bar{u} , \bar{v} , and \bar{w} are wind fields and are obtained from a GCM; λ and ϕ are the longitude and latitude, respectively; $\bar{\rho}$ is the air density, \bar{T} the temperature, C_p the specific heat at constant pressure, Γ_d the adiabatic lapse rate, \bar{P} the precipitation flux, \bar{q}_v , \bar{q}_l , \bar{q}_i the mixing ratios for water vapor, cloud water, and cloud ice, respectively, and L_c , L_d and L_f the latent heat of condensation, sublimation, and melting, respectively. Also in these equations, \bar{Q}_c , \bar{Q}_i and \bar{Q}_r represent the condensational heating rates for cloud water, cloud ice, and the radiative heating rate, respectively, \bar{P} is the rate of autoconversion from cloud droplets to raindrops, \bar{E}_r is the evaporation of rain water, \bar{S}_{BF} and \bar{S}_s are the rates of change of the mass of ice particles due to Bergeron-Findeison's process and sublimation, respectively, and \bar{w}_l and \bar{V}_T are the bulk terminal velocities for cloud water and ice particles, respectively. In addition the vertical eddy flux and horizontal diffusion terms have been denoted by F_V^x and F_H^x , respectively, where x can be \bar{T} , \bar{q}_v , \bar{q}_l or \bar{q}_i .

The cloud cover, η , is derived based on an average of the specific humidities over clear and cloudy regions in the form

$$\bar{q} = \eta q_c + (1 - \eta) q_0 , \quad (2.6)$$

where q_c and q_0 are, respectively, the specific humidity in the cloudy and clear regions. After rearranging terms, the cloud cover is given by

$$\eta = \frac{\bar{q}_v/\bar{q}_s - q_0/\bar{q}_s}{q_c/\bar{q}_s - q_0/\bar{q}_s} \quad (2.7)$$

Here, we have introduced the grid-averaged saturation specific humidity, $\bar{q}_s(\bar{T})$, which is a function of the grid-averaged temperature, \bar{T} . For a stratiform cloud, the temperature within the cloud is approximately equal to the grid-averaged temperature, i.e., $q_c = \bar{q}_s(\bar{T})$. Thus,

$$\eta = \frac{(\bar{h} - h_0)}{(1 - h_0)}, \quad (2.8)$$

where $\bar{h} = \bar{q}_v/\bar{q}_s$ is the averaged relative humidity and $h_0 = q_0/\bar{q}_s$ is referred to as the threshold relative humidity, which is a parameter to be prescribed to close the model equations.

The cloud cover expression in Eq. (2.8) denotes a linear relation between the relative humidity and cloud cover. A similar empirical relation based on observations has been developed by Smagorinsky (1960) for use in GCMs (Fig. 1). For the present large-scale studies we have used the threshold relative humidity presented in Fig. 1 for the calculation of high, middle and low cloud covers.

With the introduction of the threshold relative humidity ($h_0 < 1$), partial cloudiness in the grid box is allowed when the large-scale relative humidity is less than 100%. The cloudy area and clear region in a grid box are denoted by η and $(1 - \eta)$, respectively. Condensation occurs in the cloudy area; evaporation takes place in the clear region. Raindrops formed in a given layer are not subject to evaporation within that layer. Instead, raindrops that fall through this layer from higher clouds may evaporate in the clear region of the layer.

Since the averaged terminal velocity of cloud droplets is on the order of 1 cm/s, which is close to the large scale vertical velocity, we would expect that the terminal velocity of cloud droplets and vertical air motion roughly cancel

each other in stratiform clouds. Therefore, vertical advection of cloud LWC in Eq. (2.3) is omitted in the model calculations. The vertical eddy fluxes are calculated from a K-theory approach (Liou and Ou, 1983) and the diffusion terms in spherical coordinates are parameterized based on the methodology described by Washington and Williamson (1977).

b. Cloud Microphysical Processes

The cloud microphysical processes simulated in the present cloud model are illustrated in Fig. 2. Both the liquid and ice phase processes are included, with the liquid phase on the left-hand side and ice phase on the right-hand side of the diagram. The liquid phase processes consist of condensation of water vapor into cloud liquid water at temperatures warmer than -40°C , conversion of cloud liquid water into rain water by means of autoconversion, and precipitation of rain water onto the ground. Evaporation of cloud and rain water increases the specific humidity.

The ice phase processes include homogeneous nucleation of water condensate to cloud ice at temperatures colder than -40°C , and conversion of cloud ice to precipitation ice by virtue of gravitational settling, in which the downward ice flux is calculated by integrating the mass and fall velocity of an individual ice crystal over the whole spectrum of ice crystals. The sublimation of cloud ice increases the specific humidity. At temperatures above the freezing point, the melting process converts cloud ice to cloud water.

An important link between the liquid and ice phases is the so-called Bergeron-Findeison process. The saturation vapor pressure over ice is less than that over water. As a result, ice crystals grow by diffusion at the expense of the supercooled liquid cloud droplets. Once generated by ice nucleation, ice crystals grow by deposition due to Bergeron-Findeison's process and are depleted

by sublimation as well as the gravitational settling. Above the freezing point, clouds consist entirely of cloud water. In the region 0° to -40°C , cloud water and cloud ice may coexist. At temperatures below -40°C , cloud ice dominates because of homogeneous nucleation.

The formation of rimed crystals, such as graupel and hail, is not considered in this model since they occur more frequently in convective clouds than in large-scale stratiform clouds.

c. Numerical Implementation

In the horizontal, the grid point space is characterized by 48 equally-spaced longitudinal points and 38 Gaussian latitudes, which is the same as the horizontal grid structure used in the Air Force Geophysics Laboratory (AFGL) GCM (Yang et al., 1989). We have used this model to provide the present cloud model with initial data and a wind field. The horizontal grid space in the model has been modified near the poles to maintain nearly constant geographical distances between the grid points. In the vertical, a 16-layer stretched z-coordinate is used in the cloud model.

The upstream scheme is utilized as a means of numerically differencing the horizontal and vertical advection terms. The scheme is conditionally stable and its stability criterion follows the Courant-Friedrichs-Levy (CFL) condition, i.e., $C_{\max} \Delta t / \Delta S < 1$, where C_{\max} is the maximum velocity in the computational domain, Δt is the time step and ΔS is the grid size. This criterion is easily satisfied in large scale models. For example, in the vertical where $\bar{w}_{\max} \sim 10^0$ cm/s, $\Delta t \sim 10^3$, and $\Delta S \sim 10^5$ cm, the criterion is much less than 1. The time step used in this study is 30 minutes. The radiation calculations are updated every 3 hours, i.e., the radiative heating rates are calculated every 3 hours at every horizontal grid point.

d. Radiative Transfer Parameterization

The radiative transfer parameterization program used in this study is based on a broadband method and involves the transfer of thermal IR and solar radiation in clear and cloudy regions. In a clear atmosphere, the entire IR spectrum is divided into five bands: three for H₂O, one for CO₂, and one for O₃ absorption. The parameterizations of these broadband IR emissivities were developed by Liou and Ou (1981) and Ou and Liou (1983). The solar spectrum consists of 25 bands: six for H₂O, one for CO₂, which overlaps the H₂O 2.7- μ m band, and 18 for O₃.

In a cloudy atmosphere, low and middle clouds are treated as blackbodies in the IR radiative transfer calculation. The broadband IR emissivity, reflectivity, and transmissivity for high clouds, as well as the broadband solar absorption, reflection, and transmission values for low, middle, and high clouds, were computed based on the cloud LWC and IWC interactively generated by the cloud model. The cloud radiative properties were calculated based on the parameterizations developed by Liou and Wittman (1979). Accuracy of all the aforementioned parameterization was verified via more comprehensive and exact radiative transfer calculations described by Ou and Liou (1988).

The radiative heating rate at level z is related to the divergence of the net fluxes and is given by

$$\frac{\partial \bar{T}}{\partial t} = -\frac{1}{\rho C_p} (\Delta F / \Delta z) , \quad (2.9)$$

where Δz is the model layer thickness and ΔF is the net radiative flux difference between the layer top and bottom. This equation applies to both IR and solar heating rate calculations with downward solar flux and upward IR flux defined as positive. For the transfer of solar radiation in a cloud layer, the net flux density decreases from the cloud top to the bottom because of cloud absorption

and scattering. The absorbed radiant energy leads to the heating of the cloud layer. For black clouds (low or middle clouds), the IR radiative flux is proportional to the fourth power of the absolute temperature of the cloud. Since the atmospheric temperature usually decreases with height, the downward IR flux emitted by the atmosphere above a black cloud top is much smaller than that emitted upward by the black cloud. As a result, the net flux near the cloud top is greater than zero and leads to strong IR cooling in the region. Similarly, there is IR heating near the cloud bottom.

Specification of the overlap that occurs between cloud layers is required for the calculation of radiative transfer in a radiation model. In this study, the model-generated clouds are strapped into three cloud decks. Low, middle, and high clouds fill, respectively, layers (4,5,6), layers (7,8), and layers (9,10). The cloud cover for each deck of clouds is obtained by averaging model cloud covers as follows:

$$\eta_l = (\eta_4 + \eta_5 + \eta_6) / 3 , \quad (2.10a)$$

$$\eta_m = (\eta_7 + \eta_8) / 2 , \quad (2.10b)$$

$$\eta_h = (\eta_9 + \eta_{10}) / 2 , \quad (2.10c)$$

where η_l , η_m and η_h denote deck cloud covers for low, middle, and high clouds, respectively.

To determine the total cloud amount, we have assumed that clouds overlap each other in a statistically random manner. Thus the total cloud cover is given by

$$\eta = 1 - (1 - \eta_l)(1 - \eta_m)(1 - \eta_h) , \quad (2.11)$$

where η is the total cloud cover over a grid area. For partly cloudy conditions, the radiative heating/cooling rate at each model layer is obtained by linearly weighting the percentages of the total cloud cover, η , and clear portion, $(1 - \eta)$, in the form

$$\left(\frac{\partial \bar{T}}{\partial t}\right)^{pc} = \eta \left(\frac{\partial \bar{T}}{\partial t}\right)^c + (1 - \eta) \left(\frac{\partial \bar{T}}{\partial t}\right)^{nc}, \quad (2.12)$$

where the superscripts pc, c, and nc represent partly cloudy, cloudy, and clear conditions, respectively.

3. BULK PARAMETERIZATION OF CLOUD MICROPHYSICS

Since it is not practical in a large-scale cloud model to simulate detailed microphysical processes with respect to each individual cloud particle, we must relate these processes in terms of bulk quantities, which represent the various sources and sinks for cloud water substances.

a. Liquid Phase

(i) Condensation

Condensation occurs as a result of expanding air under saturation conditions and may be related to the time rate of change of the saturation vapor pressure. Consequently, the condensational heating rate may be derived from the first law of thermodynamics, the Clausius-Clapeyron equation and the hydrostatic approximation as follows:

$$\bar{Q}_c = \eta \Gamma_d \frac{\bar{q}_s(\bar{T})}{R_a} \left(\frac{LR_a - C_p R_v \bar{T}}{C_p R_v \bar{T}^2 + \bar{q}_s L^2} \right) \bar{w}, \quad (3.1)$$

where Γ_d is the dry adiabatic lapse rate, R_a is the gas constant for air, R_v is the gas constant for water vapor, L is the latent heat for liquid and vapor phases, and \bar{q}_s is the saturation vapor pressure. The condensation is strongly dependent on the vertical velocity, \bar{w} . As saturated air rises, i.e., $\bar{w} > 0$, condensation takes place and cloud forms, while depletion of clouds occurs with descending saturated air.

(ii) Autoconversion

Autoconversion is a process through which small cloud droplets merge into large raindrops. The parameterization of autoconversion follows the simple exponential form developed by Sundqvist (1978):

$$\bar{P} = c_0 \bar{q}_l (1 - \exp[-(\bar{q}_l / (\eta q_{l,r}))^2]) , \quad (3.2)$$

where c_0 denotes the typical time for the conversion of droplets to raindrops, and $q_{l,r}$ is a reference value of cloud LWC above which the conversion from cloud droplets to raindrops increases rapidly.

(iii) Evaporation of raindrops

The evaporation of raindrops may be derived from the combination of the Fick law of mass diffusion and the Marshall-Palmer raindrop size distribution. The size distribution is assumed to remain the same throughout the whole process of evaporation. The raindrop evaporation rate is given by

$$\bar{E}_r = K_e (1 - \bar{h}) \bar{P}^{0.42} . \quad (3.3)$$

where the evaporation rate constant K_e is $1.785 \times 10^{-2} \bar{q}_s$.

b. Ice Phase

The ice phase parameterizations include homogeneous/heterogeneous nucleation to generate ice crystals, depositional growth to simulate the Bergeron-Findeison process, sublimation and melting of ice crystals, and gravitational settling to deplete the ice crystals. The Bergeron-Findeison process occurs primarily at temperatures between 0° and -40°C , while below -40°C homogeneous nucleation dominates. The parameterizations of these source and sink terms are described below.

(1) Homogeneous nucleation

Homogeneous nucleation takes place whenever condensation occurs at temperatures below -40°C . Homogeneous nucleation is analogous to the liquid water condensation process, and may be written in the form

$$\bar{Q}_i = \eta \Gamma_d \frac{\bar{q}_s(\bar{T})}{R_a} \left(\frac{L_d R_a - C_p R_v \bar{T}}{C_p R_v \bar{T}^2 + \bar{q}_s L_f^2} \right) \bar{w}, \quad (3.4)$$

where L_d is the latent heat for ice and vapor phases.

(ii) Heterogeneous nucleation

Heterogeneous nucleation leads to the formation of ice crystals on active ice nuclei primarily at temperatures between 0° and -40°C . Based on the experimental work of Mason (1971) and Koenig and Murray (1976), it is assumed that the active ice-forming nuclei (IN) concentration may be expressed in terms of temperature as follows:

$$N = A_1 \exp \left\{ -\frac{\ln(10)}{A_2} \max[(T - T_0), T^*] \right\}, \quad (3.5)$$

where $A_1 = 1$, $A_2 = 4$, $T^* = 0^\circ\text{C}$, and T_0 is a threshold temperature, which is taken to be -20°C . Here, it is assumed that when the saturated air temperature is lower than T_0 , the total number of IN remains the same as that at T_0 .

The heterogeneous nucleation rate of ice crystals, S_h , is given by

$$S_h = m_0 \frac{dN}{dt}, \quad (3.6)$$

where m_0 is the mass of a newly nucleated ice crystal, prescribed as 10^{-11} grams, which is equivalent to an ice sphere with a diameter of $2.77 \mu\text{m}$ (Koenig and Murray, 1976), and

$$\frac{dN}{dt} = \begin{cases} \frac{N_{t+\Delta t} - N_t}{\Delta t} & \text{if } T \geq -20^\circ\text{C} \\ 0 & \text{if } T < -20^\circ\text{C} . \end{cases} \quad (3.7)$$

Here, $N_{t+\Delta t}$ and N_t are the IN concentrations at consecutive time steps of $t + \Delta t$ and t , respectively.

(iii) Bergeron-Findeison process

The Bergeron-Findeison process transforms cloud water into cloud ice at temperatures between 0° and -40°C. To simplify the complicated vapor diffusion equation, Koenig (1971) developed a simple equation to describe the crystal vapor diffusion growth rate as a function of mass. The equation is written as follows:

$$\frac{dm}{dt} = a_3 m^{a_4}, \quad (3.8)$$

where a_3 and a_4 are temperature-dependent parameters given in Koenig (1971), and m is the crystal mass in grams.

The bulk quantity of the ice crystal depositional rate, denoted as S_{BF} , may be derived from Eq. (3.8) by multiplying both sides by N , as follows:

$$\bar{S}_{BF} = \frac{d}{dt} (\bar{\rho} \bar{q}_i) = \eta f_l N^{1-a_4} a_3 (\bar{\rho} \bar{q}_i)^{a_4}, \quad (3.9)$$

where $f_l = \bar{q}_l / (\bar{q}_l + \bar{q}_i)$ is the cloud liquid fraction serving as an adjustment factor, which allows for higher ice crystal growth rates with more cloud water. The growth is terminated if there is no cloud water to supply water vapor.

(iv) Sublimation and melting of ice crystals

Similar to the derivation for the evaporation of raindrops, we have developed the following equation for the rate of sublimation:

$$\bar{S}_s = 0.1037 (\bar{\rho} \bar{q}_s) (1 - \bar{h}) (\bar{\rho} \bar{q}_i)^{0.65}. \quad (3.10)$$

At temperatures above 0°C, cloud ice crystals are assumed to melt instantaneously.

(v) Gravitational settling

Gravitational settling is an important sink for cloud IWC. Therefore, it is desirable to have a representative (mean-volume-weighted) downward flux of ice water. Following Starr and Cox (1985), the downward ice flux may be expressed as

$$\bar{V}_T(\bar{\rho} \bar{q}_i) = \int_{L_{\min}}^{L_{\max}} n m v dL, \quad (3.11)$$

where n , m , and v are the ice crystal size distribution, mass and terminal velocity of an ice crystal, respectively, and L is the maximum dimension of an ice crystal. L_{\min} and L_{\max} are the minimum and maximum sizes of ice crystals. The cloud IWC may be further related to n and m as

$$\bar{\rho} \bar{q}_i = \int_{L_{\min}}^{L_{\max}} n m dL. \quad (3.12)$$

In order to calculate the downward ice flux, the size distribution, mass, and terminal velocity for the precipitating ice crystals need to be specifically expressed in terms of the maximum dimension of ice crystals.

The size distributions of ice crystals in mid-latitude cirrus clouds have been measured from aircraft using an optical probe (Heymsfield, 1977). Using these data, Heymsfield and Platt (1984) have averaged all spectra of crystals within every 5°C temperature interval ranging from -20°C to -60°C. The ice crystal size distributions in terms of the maximum dimension of ice crystals may then be parameterized for different temperature ranges in the form

$$n = a_n L^{b_n}, \quad (3.13)$$

where a_n and b_n are temperature dependent empirical coefficients.

The minimum length that the optical probe can measure is about 20 μm . Small ice crystals less than 20 μm in size could be missed by the measurement technique. Consequently, small ice crystal data were excluded from the analysis by Heymsfield and Platt (1984). For this reason, 20 μm is taken as the minimum length of ice crystals, L_{\min} , which is needed in the calculations of Eqs. (3.11) and (3.12).

(vi) Crystal mass and terminal velocity

The individual ice crystal mass, m , may be parameterized in terms of the maximum dimension of an ice crystal, L , as follows:

$$m = a_m L^{b_m}, \quad (3.14)$$

where m and L are in units of grams and μm , respectively. The constants a_m and b_m associated with various ice crystal habits are given in Heymsfield (1972).

The terminal velocity v in m/s of an ice crystal of maximum dimension, L , in μm is given by

$$v = a_v L^{b_v}, \quad (3.15)$$

where the constants a_v and b_v are dependent on the ice crystal habit and size as given in Starr and Cox (1985). These coefficients were derived at an ambient pressure of 400 mb. For an ice crystal at a given pressure p , Beard and Pruppacher (1969) have suggested that its terminal velocity may be expressed by

$$v(p) = v(p_*) (p_*/p)^{1/3}, \quad (3.16)$$

where p_* denotes a reference pressure level, and $v(p_*)$ is the terminal velocity of a crystal at the reference level. To obtain the terminal velocity at any given pressure, we simply apply the pressure adjustment to the expression in Eq. (3.15).

(vii) Downward ice flux

The ice crystal size distribution, ice crystal mass, and terminal velocity are all parameterized in terms of the maximum dimension. Thus, the downward ice flux may be obtained by analytically integrating Eq. (3.11), provided that the size of the largest crystal, L_{max} , is known. Since the lower limit, L_{min} , is set to be 20 μm , as stated previously, the upper limit (L_{max}) may be determined from Eq. (3.12) as follows: We first obtain $\bar{\rho q}_i$ for the n th time step. Subsequently,

Eqs. (3.13) and (3.14) are substituted into Eq. (3.12) to calculate L_{\max} . Having determined L_{\max} , the downward ice flux can then be computed from Eq. (3.11) in the form

$$\overline{V_I(\rho q_i)} = \frac{a_n a_m a_v}{b_n + b_m + b_v + 1} [L_{\max}^{(b_n + b_m + b_v + 1)} - L_{\min}^{(b_n + b_m + b_v + 1)}] \quad (3.17)$$

The downward flux is a function of L_{\max} , which in turn is a function of cloud IWC.

4. MODEL PERFORMANCE AND VERIFICATION

a. Model Input and Verification Datasets

The atmospheric data generated from the AFGL spectral global model (Yang et al., 1989) analyzed at 12Z July 1-4, 1979, were used as inputs to the cloud model. This period has been chosen because of the availability of cloud and radiation budget data that have been analyzed on a daily basis. The input data contain temperature, specific humidity, and wind fields (\bar{u} , \bar{v} , \bar{w}) at all 12 σ -layers in the atmosphere, plus the surface pressure and geopotential height. These analyses were carried out using a rhomboidal 15 (R15) truncation which corresponds to a horizontal resolution of 38 and 48 grid points in latitude and longitude, respectively. In the vertical, since the GCM-generated input data are available only at the σ -coordinate, it is necessary to perform vertical interpolations to obtain these data in the z -coordinate.

The 3DNEPH cloud data sets have been determined from various satellite, aircraft and ground-based observational sources. Based on 3DNEPH analysis, the global cloud climatologies for January and July 1979 have been processed into appropriate formats for model verification (Koenig et al., 1987). The global distribution of cloud amounts on July 1-4, 1979 is derived from the above cloud climatologies and used as the verification dataset for the cloud cover simulated

in the model.

It is important to recognize the limitation of 3DNEPH cloud analysis. A threshold method is employed to process satellite images to determine cloud cover by a threshold temperature. If an observed brightness temperature of a pixel is colder than the threshold temperature, then a cloudy condition is assigned to the pixel. Consequently, the cloud amount tends to be overestimated when the associated surface temperature is low, and underestimated when a temperature inversion is located in the region. This is evident from the fact that 3DNEPH over- and underestimates cloud amounts in the wintertime and summertime polar regions, respectively (Henderson-Sellers, 1986). However, several intercomparisons of the cloud cover between 3DNEPH and the other cloud retrieval techniques have been made (Koenig et al., 1987; Hughes, 1984). The 3DNEPH total cloud cover appears to be reliable, except in the polar regions where all satellite retrieval methodologies tend to fail. Additionally, the surface observational cloud climatology compiled by London (1957) is used as a complementary verification dataset for the polar regions.

The archived ERB flux data tapes for July, 1979, provided by the NASA ERB team (Kyle et al., 1990), are used to validate OLR produced by the model. Since ERB fields are strongly modulated by the radiative effects of clouds, including cloud cover and cloud LWC/IWC, they have been widely used in large-scale cloud model verifications (Slingo, 1987; Smith, 1990). Monthly mean distributions of liquid water have been derived from the Nimbus 7 SMMR observations over the oceans for the period November 1978 to November 1979 (Prabhakara and Short, 1984). The liquid water estimate for July 1979 is applicable to the monthly average over an area approximately 3° by 5° . The liquid water derived from satellite microwave channels includes vertically integrated amounts of liquid

droplets in both clouds and rain. The liquid water verification data are confined to the oceans equatorward of 60° latitude. Over land and ice surfaces, due to the limitation of microwave techniques, there is no climatological liquid water data of global extent for comparisons.

Since there is no ground truth with which to compare, the accuracy of liquid water observations from SMMR is roughly estimated as 100 g/m², based on theoretical considerations (Prabhakara et al., 1983). However, by taking monthly averages, this accuracy may be improved to 50 g/m² (Prabhakara and Short, 1984).

b. Design of the Verification and Initial Data

In the development of any parameterization scheme, the prediction results must be carefully verified to assess its performance. The large scale cloud model was integrated for 96 hours with a time step of 30 minutes from the initial conditions taken at 12Z on July 1, 1979. The wind fields are prescribed from a GCM. It is noted that cloud-radiation feedback to the dynamic structure is not accounted for in this study.

With input of the initial data and wind fields, the cloud model is capable of forecasting large-scale cloud cover and cloud LWC/IWC, which are interactively used in the radiation model. The radiation model computed OLR for comparison with the ERB satellite data. In this study, the interactive radiation computations are undertaken every 3 hours, while the calculated heating/cooling rates are input in the cloud model at every time step during those 3 hours.

The simulated cloud cover, OLR, cloud LWC and cloud IWC are verified against 3DNEPH cloud cover, ERB data, SMMR results, and in situ observations and other model studies, respectively. However, there are several problems which make the use of satellite observations in model verification not entirely straightforward. For instance, verification datasets such as 3DNEPH and ERB are

based on the daily average over local time, while the output of the model simulation is the instantaneous global distribution. Allowing intercomparisons to be made between the satellite observations and model simulations, we have to average the model predicted fields over local time in order to obtain daily averaged model results.

The analysis data on 12Z, July 1, 1979 for temperature and specific humidity are used as initial values to perform a 96-hour model simulation. Data for the cloud LWC/IWC are not available for initial values on a global basis. At this point we do not have any physical means to provide the initial cloud LWC/IWC values. For this reason, we have set these values as zero, initially. Unless specified, all of the results including satellite observations and model simulation are averaged over July 3-4, 1979. That is, most of the results shown in this and latter sections are presented as a 2-day average of July 3 and 4. Due to the limitation of the initial cloud LWC/IWC fields, the results for July 1 and 2 have not been included in the analysis and verification.

c. Model Results and Verification

In Fig. 3a, the model-predicted zonal mean total cloudiness, averaged over July 3-4, is compared with the corresponding 3DNEPH cloud data. Differences between the two curves are generally within 10% of the total cloud cover except in the tropics, Arctic, and Antarctic areas.

As mentioned in Subsection 4a, 3DNEPH under- and overestimates cloud covers in Arctic and Antarctic regions, respectively, during the Northern Hemisphere summer. Henderson-Sellers (1986) compared 3DNEPH monthly mean data with London's (1957) cloud climatology which is based on surface cloud observations. Since London's cloud climatology was compiled only for the Northern Hemisphere, the comparison is confined to the Northern Hemisphere. London's cloud climatology

shows about 70% of total cloudiness in the summertime Arctic region and 40% in the wintertime. The 70% of total cloudiness in the Arctic is close to our model prediction in the area. This explains the differences between the predicted and 3DNEPH cloud cover in the Arctic and Antarctic regions.

The observed large cloudiness in the tropics is largely caused by tropical anvils, which originate from convective clouds. Since the present large-scale cloud model has been developed primarily for stratiform clouds, the simulated cloud cover in the tropics is underestimated, as is evident in Fig. 3a. Another shortcoming in the simulated cloud cover is the overestimation of cloud cover near 60° S, where the absorbed solar radiation becomes smaller. As a result, strong radiative cooling is produced at the top of middle clouds, leading to a large increase of total cloudiness in the region. It appears that an improvement could be made if a dynamic instability feedback were allowed in the simulation. The simulated small cloud cover located at the subtropic highs in both hemispheres is realistic. Large cloudiness in the tropics is also predicted, although the 3DNEPH cloud data suggests that the predicted cloud cover is underestimated.

Figure 3b reveals good agreement in OLR between the model simulation and ERB observation, with differences generally less than 10 W/m², except in the tropics. The OLR in the tropics predicted from the model is 30 W/m² higher than that analyzed from the ERB data. This overestimation of OLR may be explained by the following two factors. First, the altitude of high clouds defined in the model is usually lower than the actual height of tropical anvils. Second, the simulated cloud cover in the tropics is underestimated. Both curves in Fig. 3b indicate two maxima located in the subtropics in both hemispheres with a minimum in the tropics. These two well-defined OLR maxima are associated with the subtropical highs, where small cloudiness coupled with high temperature produces

large OLR. The minimum OLR in the tropics is related to the ITCZ region, where thick high clouds are abundant.

Data on cloud LWP are very limited. There are no observational LWP data on a daily basis with which to compare, nor are the zonal averaged values of LWP available for July of 1979. Since the time domain in this study is the very beginning of July, we have compared the predicted zonal mean LWP with the monthly averaged zonal mean data analyzed from SMMR for June, 1979. Figure 3c shows the zonal mean LWP from model simulations and from SMMR measurements taken from Prabhakara and Short (1984). The zonally averaged LWPs over the oceans are shown in the figure. The zonal mean simulated cloud LWPs compare quite well with SMMR observations. Differences between the two are within 50 g/m^2 which is the uncertainty of SMMR data suggested by Prabhakara and Short.

The maximum LWP that occurs in the tropics is related to the ITCZ. The two well-defined local LWP maxima at mid-latitudes in both hemispheres are associated with storm tracks. The minimum LWP is found in regions of subtropical highs with prevailing downward motions. The SMMR data show maximum values of about 140, 47, and 40 g/m^2 in the tropics and mid-latitudes, respectively. The corresponding values obtained from simulation are 130, 53, and 65 g/m^2 , respectively. The ratio of maximum observed LWP in the tropics to that in the middle latitude is about 3 to 1. This ratio is about 2 to 1 based on the model simulation. This difference indicates that the model underestimates the cloud LWP in the tropics, where a significant amount of LWP observed by the SMMR is associated with convective clouds, which are not simulated in the present model.

The predicted cloud cover, OLR and LWP in the following figures are presented in terms of the horizontal cross-sections to demonstrate the geographical distribution of cloud fields. Cloud cover and OLR are illustrated

by the gray shades in which the intensity in the picture is proportional to a certain range of data values.

Figures 4a and 4b show the geographical distribution of cloud cover determined from observation and simulation, respectively. The corresponding gray shade values are depicted in the lower right-hand corner. The brighter the cloud picture, the larger the cloud cover is.

The major distinctive features of the geographical distribution of cloud cover depicted in the observation and simulation include the following. First, a pronounced bright band of cloudiness extends along the ITCZ from 150° W to 90° E. This cloud band splits into two bands. The north branch spreads into southern Asia and the northwestern Pacific, the south branch expands southeast to the southwestern Pacific. The north band is associated with the seasonal monsoon, while the south band is related to the Southern Pacific Convergence Zone (SPCZ). Although the ITCZ cloud band is less pronounced in the simulation, the model reasonably predicts the bright cloud bands extending from the central Pacific to the central Atlantic, and into central Africa.

Second, areas of small cloudiness, i.e., a dark cloud picture, associated with subtropical highs occur both north and south of the ITCZ. For example, the small cloud covers over southern Africa, Europe and Middle-East Asia, and North and South America are clearly identified in both the observation and the simulation. The oceanic subtropical highs in the Atlantic and Pacific Oceans are also evident from the presence of small cloudiness over the regions.

Third, the large bright cloud bands in the mid-latitudes of both hemispheres are associated with the mid-latitude storm tracks. In both the simulation and the observation, bright cloud bands are found over the east coast of South America, the southern and northern Pacific, and the Greenland Sea. The

cloudiness over the east cost of North America is larger in the simulation than in the observation.

Finally, the under- and overestimation of cloud cover is shown in the 3DNEPH data in the Arctic and Antarctic regions, respectively, for the Northern Hemisphere summer. Comparing Figs. 4a and 4b, it is evident that the cloud picture over the Antarctic area is brighter in the observation than in the simulation, and vice versa for the Arctic region.

Figures 5a and 5b show the OLR obtained from observation and simulation, respectively. The intensity of the gray shades, given in the lower right-hand corner of each figure, is defined such that the brighter the picture, the smaller the radiative flux is. There are two distinct features on these maps. First, the well defined ITCZ and monsoon circulation are characterized by bright regions, i.e., relatively small values of OLR. They are located over the equatorial western and eastern Pacific, the Atlantic and central Africa, as well as the monsoon area over India and Asia. As mentioned previously, the cloudiness in these regions is underestimated in the simulation. As would be expected, the flux values in these regions are overestimated by the model. Second, the almost continuous dark belts are associated with the subtropical highs located to the south and north of the ITCZ. In these regions, large OLR values are due to the small cloudiness in the areas. Small flux values are also evident in the mid-latitude storm tracks in the Northern Hemisphere. However, the simulated values of OLR in the Greenland Sea, near 70° N and 0° E, appear to be too small in comparison with observation.

Figures 6a and 6b illustrate the geographical distribution of LWP derived from observation and simulation, respectively. The observed data taken from Prabhakara and Short (1984) are displayed in terms of the monthly averaged map

for July, 1979. In Figs. 6a and 6b, a large amount of liquid water in the ITCZ is evident. However, in the subtropical highs of both hemispheres, liquid water is small. In the southern Pacific, the model simulates large LWPs, which are also evident in the observed values. In both the simulation and the observation, abundant liquid water is found over the Indian Ocean, and southeast and northeast Asia. In addition, the well-defined observed local LWP maxima near the east coasts of North, Central, and South America are well simulated by the model. Local LWP minima observed west of Africa, and South and North America are also shown in the simulation.

The large amount of liquid water associated with the mid-latitude storm tracks near 50° S(N) - 60° S(N) is not shown in the SMMR observation because the sea surfaces are largely covered by ice. In addition, the model simulates large amounts of liquid water over land in Central America, central Africa, India and southeast China. These results are not reported by the SMMR observation because of the inability of the microwave technique to function over land. From the above comparisons, it appears that the geographic distribution of LWP is well simulated in the present model.

Since observed cloud IWC has not been available on the global scale, we qualitatively compare the model-predicted cloud IWC with values derived from aircraft measured data in cirrus, as well as with other model results. Based on aircraft measured data in mid-latitude cirrus over the United States, Heymsfield and Platt (1984) have derived the ice crystal size distribution and IWC as functions of temperature. Averaged cloud IWC varies from 0.001 g/m^3 at temperatures below -40°C to about 0.02 g/m^3 above this temperature. Similar cloud IWC values have also been simulated from a cirrus cloud model by Starr and Cox (1985). The simulated cloud IWC, averaged over July 3-4, 1979, is shown in

Fig. 7. The magnitude of the predicted cloud IWC is on the order of 0.01 g/m^3 , which is consistent with the aforementioned model simulation and aircraft observed values in mid-latitude cirrus clouds.

The maxima cloud IWC are located along a temperature of about -15°C , at which the maximum rate of Bergeron-Findeison's process occurs. The simulated cloud IWC decreases from about 0.01 g/m^3 near -15°C to 0.001 g/m^3 at temperatures below -40°C . The variations of cloud IWC with respect to the temperature obtained from the model are similar to those suggested by Heymsfield and Platt (1984). It is noted that the simulated cloud ice vanishes at temperatures warmer than the melting point, because the melting process converts ice crystals into water droplets. The simulated cloud IWC appears to depend more on temperature than on vertical velocity, which is most significant in the condensation process. The latitudinal distribution of cloud IWC appears to be realistic. In the wintertime Antarctic area, all clouds contain ice, while in the summertime Arctic region, only middle and high clouds are ice clouds. In the tropics, high clouds are largely composed of ice crystals.

5. THE ROLE OF RADIATIVE HEATING AND ICE PHASE PROCESSES IN CLOUD FORMATION

In order to examine the effects of radiative heating fields and ice phase microphysics on the large-scale cloud simulations, a set of numerical experiments has been carried out with and without the inclusion of radiative heating and ice phase processes. Below is a brief description of the experimental runs:

- CTRL: Control run which includes both radiation and ice-phase processes.
- EXP1: As in CTRL, but without radiative heating.
- EXP2: As in CTRL, but without the ice-phase processes.

All of the control and experimental runs have the same initial conditions and

wind fields. The results are averaged over the same period, allowing intercomparisons to be made between the control and experimental runs.

a. Control Run

The control run is identical to the experiment described in Section 4b. In that section, the computational results were illustrated in terms of the horizontal cross section. In this section, these results are shown in terms of the meridional cross section so that the vertical structure of cloud fields can be easily identified.

Figures 8a and 8b show the zonally averaged cloud cover and cloud LWC predicted from the model CTRL. Cloud IWC predicted from CTRL has been shown in Fig. 7. Three cloud cover maxima are seen in the tropics and in the mid-high latitudes of both hemispheres. These maxima are due to large upward motions in these regions. Minima cloud covers occur in the regions of subtropical highs, which are directly related to downward motions. Because of the strong sinking motion of the Southern Hemisphere Hadley cell, cloud cover in the subtropical high of the Southern Hemisphere is smaller than that in the Northern Hemisphere counterpart.

The pattern of simulated cloud LWC in Fig. 8b is consistent with that illustrated in Fig. 8a. The three cloud LWC maxima, located in the tropics and mid-latitude storm tracks, correspond to large cloudiness in these regions. The cloud LWC minima associated with the subtropical highs are due to the prevailing downward motions in the regions. In the vertical, large cloud LWCs are associated with low and middle clouds. The maximum cloud LWC is located in the tropics, and two local maxima exist in mid-latitudes.

b. Experiment on Inclusion of Radiative Heating

Figures 11-13 show the results from the experiments with and without the

inclusion of radiative heating. These results are expressed in terms of the differences between two experiments (CTRL-EXP1).

Solar heating rate differences are illustrated in Fig. 9a. Solar radiation heats the atmosphere. As would be expected, the solar heating rates in July of the Northern Hemisphere are much larger than those of the Southern Hemisphere counterpart. There is no solar radiation within the Antarctic Circle because the sun does not rise above the horizon in this region during July. Two solar heating maxima with values of ~ 2 K/day are located at the tops of middle clouds in the Northern Hemisphere. Large solar heating rates within the Arctic Circle are due to long solar days. Large solar heating rates in the tropics are related to small solar zenith angles during the daytime. The large solar heating located in the upper atmosphere is associated with strong ozone absorption.

Figure 9b shows the IR heating rate differences. The most distinct feature in this figure is the strong IR cooling rates that occur at the middle cloud tops. This is because high clouds are considered to be nonblack in radiation calculations, while middle clouds are assumed to be blackbodies. As a result, the upward IR flux emitted by middle clouds is much stronger than the downward flux emitted by high clouds. Consequently, strong IR radiative cooling is generated at the tops of middle clouds.

The inclusion of IR radiative heating basically cools the atmosphere. However, if low cloudiness is sufficiently large to emit strong downward IR fluxes from the cloud base, weak IR heating may be produced beneath the cloud base. This explains the two regions of weak IR heating at the low cloud bottoms at 60° S and in the tropics. Two other weak IR heating rates, located in the upper tropical atmosphere and in the lower atmosphere in the Arctic, are associated with the areas of high ozone concentration and temperature inversion

in the regions, respectively.

Figure 10a shows net radiative heating rates. The inclusion of the radiative processes in the model decreases the atmospheric temperature. As would be expected, the net radiative heating shows relatively large cooling at middle cloud tops and small cooling at cloud bottoms. However, there are weak heating rates in lower tropical atmospheres and in the Southern Hemisphere due to large low cloud cover over those regions. The strongest radiative cooling at the middle cloud top, located within the Antarctic Circle, is due to the absence of solar radiation in the winter season. Relatively large cooling at the low cloud level within the Arctic area is associated with the temperature inversion in the region, while the large cooling near the surface layers in the equatorial region is due to the contribution of water vapor continuum absorption. It is noted that noticeable net radiative heating is located in the upper atmosphere in the Northern Hemisphere because of the ozone solar absorption in the region. The weak heating at the middle cloud level within the Arctic Circle is due to the absorption of solar radiation during long solar days.

Figure 10b shows the temperature pattern. The inclusion of radiative heating decreases the atmospheric temperature which decreases more significantly for cloudy conditions than clear sky. The largest temperature reduction occurs at the middle cloud top near 66.5°S , where the sun does not rise much above the horizon in the winter season. Temperature decreases are relatively small in the subtropical regions where small cloud amounts are located. These temperature changes, in turn, initiate all of the changes in the cloud fields such as cloud cover, cloud LWC, and cloud IWC.

Figure 11a shows differences in cloud cover between the two experiments. The inclusion of radiative heating leads to an increase in cloud cover. Large

increases occur at the middle cloud tops, at which large temperature decreases are located. The increases in low cloudiness are relatively small due to small radiative cooling associated with low clouds. However, there are two large increases of low cloud cover. One occurs in the tropics where a large amount of water vapor exists, while the other is in the Arctic area where a strong inversion is located.

Figure 11b illustrates the differences in total cloud water content, i.e., cloud LWC plus IWC between CTRL and EXP1. Cloud water increases wherever cloud cover increases. As has been mentioned previously, the decrease of cloud temperature by radiative cooling increases the condensational rate and results in the increase of total cloud water. The large increase of cloud water occurs at the tops of middle and low clouds in the tropics, where strong radiative cooling is located.

c. Experiment on Ice Phase Processes

Figures 12a and 12b show the results from the experiments with and without the inclusion of ice-phase processes. The differences in temperature and cloud cover due to the inclusion of ice-phase processes are insignificant. Figure 12a illustrates the differences in cloud LWC between the cases with and without the inclusion of ice-phase processes. This figure shows little change in cloud LWC in the tropical low and middle clouds that contain primarily water droplets. Marked reductions of cloud LWC with ice processes included occur in low, middle, and high clouds within the Antarctic Circle, high clouds in the tropics, and middle and high clouds within the Arctic Circle. In these regions clouds are largely composed of ice crystals, which deplete the cloud LWC by virtue of Bergeron-Findeison's process. Since there is no cloud IWC in EXP2, the differences in cloud IWC are identical to cloud IWC shown in CTRL (see Fig. 7).

Figure 12b shows the differences in total cloud water content. The increases of total cloud water when the ice phase is included indicate that the increase of ice crystals in clouds is larger than the reduction of cloud LWC. It follows that ice clouds in these regions are not entirely controlled by Bergeron-Findeison's process.

In order to further examine the relationship between autoconversion and Bergeron-Findeison's process on cloud formation, we have undertaken two more experimental runs with the autoconversion rate of $c_0 = 10^{-6} \text{ sec}^{-1}$, which is five times smaller than what was used in the CTRL. A smaller autoconversion rate leads to the production of more cloud LWC, which in turn generates more cloud IWC through Bergeron-Findeison's process. In the following two experimental runs, the first run is the same as CTRL with the smaller value of the autoconversion rate, i.e., $c_0 = 10^{-6} \text{ sec}^{-1}$; the second run is the same as the first run but without the ice phase processes.

Figure 13a shows a pattern very similar to that in Fig. 12a. Due to the smaller value of the autoconversion rate, the differences in cloud LWC are about five times larger in Fig. 13a than they are in Fig. 12a. The large differences in cloud LWC indicate that a strong Bergeron-Findeison process takes place when there is more cloud LWC. However, the values of cloud IWC in Fig. 13b are close to those in Fig. 7, even though Bergeron-Findeison's process is much stronger in the former than in the latter. This indicates that the downward ice flux is larger in the former than in the latter.

Figure 13c shows the differences in total cloud water content for the smaller c_0 . The total cloud water content decreases in the region where ice clouds are present. The reduction of the total cloud water content is mainly controlled either by autoconversion that converts cloud LWC into precipitation

or by gravitational settling that removes ice crystals from the cloud layer. The decrease of total cloud water content when the ice phase processes are included indicates that gravitational settling is an efficient mechanism for reducing the cloud IWC.

6. CONCLUSIONS

A time-dependent, three-dimensional, large-scale cloud-moisture model has been developed for the prediction of temperature, cloud cover, cloud LWC, cloud IWC, and precipitation. Partial cloudiness is allowed to form when the large-scale relative humidity is less than 100%. The cloud microphysical processes simulated in the model include both liquid and ice phases, which are physically included for the first time in a large-scale cloud model to simulate cirrus clouds.

A 96-hour model simulation, with the initial conditions taken at 12Z on July 1, 1979 has been carried out to assess the performance of the large-scale cloud model. The comparisons between the model simulation and the satellite observations indicate the large-scale cloud model is capable of realistically simulating zonal means and geographical distributions of cloud fields, including cloud cover, OLR and net solar flux at TOA, and cloud LWC. Differences in the zonal mean total cloud cover between the simulation and the 3DNEPH data are generally within 10%. Generally, the simulated zonal mean OLRs are within 10 W/m^2 of the ERB results. The zonal mean values of simulated cloud LWP compare quite well with the SMMR observations, with differences being less than 50 g/m^2 , which is the uncertainty of the SMMR data. However, it is clearly indicated that the model underestimates cloud cover and cloud LWC and overestimates the OLR in the tropics, where clouds are predominantly convective clouds, which are not

simulated in this model. In the geographical distributions of cloud fields, the large-scale cloud model has simulated the large cloud bands in the ITCZ, monsoon areas, Southern Pacific Convergence Zone, and the mid-latitude storm tracks, although the ITCZ cloud band is less pronounced in the simulation. At the subtropical highs, areas of small cloudiness over southern Africa and northern Africa, and North and South America are clearly identified in both of the observations and the model simulation. The magnitude of the cloud IWC in the simulation is about 0.01 g/m^3 , which is consistent with the aircraft measurements in cirrus clouds, as well as with other model results. The simulated cloud IWC appears to depend more on temperature than on vertical velocity, which is critical to the condensational process.

The model-simulated cloud fields are strongly linked to large-scale circulations. Inspecting the model-predicted cloud fields, such as cloud cover, OLR, and cloud LWC, we find that these cloud properties are closely related to one another. Large amounts of cloud cover coincide with abundant cloud LWC, which generates large precipitation rates by virtue of the autoconversion process simulated in the model. In summary, the atmospheric moisture and cloud fields are linked together by the cloud microphysical processes simulated in the cloud model. More importantly, the moisture, cloud fields and earth's radiation budget are physically related to large-scale thermal and dynamical structures, such as temperature and vertical velocity.

Sensitivity studies have been performed to examine the effects of radiative heating fields and ice-phase cloud microphysics on large-scale cloud formation. The inclusion of radiative processes in the cloud formation model significantly decreases the cloud temperature, with the strongest cooling occurring at the middle cloud top. However, there may be weak heating located in a low cloud if

cloud cover is sufficiently large to produce a strong downward flux. The decrease of temperature by radiative cooling increases the atmospheric relative humidity and condensation in clouds. As a result, cloud cover and total cloud water, including cloud LWC and IWC, increase due to the inclusion of radiative processes.

The inclusion of ice-phase processes has a greater effect on the cloud LWC and IWC than on the temperature and cloud cover fields. If the cloud LWC is large enough to undertake an effective Bergeron-Findeison's process, the total cloud water content decreases, with large decreases located at the regions where the presence of ice clouds is most pronounced. The reduction of the total cloud water content is mainly controlled either by autoconversion, which converts cloud LWC into precipitation, or by gravitational settling, which removes ice crystals from the cloud layer. The decrease of total cloud water content when the ice-phase processes are included indicates that gravitational settling is an efficient mechanism for reducing the cloud IWC.

Acknowledgments. The research work contained in this paper has been supported by the Air Force Office of Scientific Research Grant AFOSR-91-0039. We thank Professor H. Sundqvist for helpful comments on the paper.

REFERENCES

- Beard, K.V., and H.R. Pruppacher, 1969: A determination of the terminal velocity and drag of small water drops by means of a wind tunnel. J. Atmos. Sci., 26, 1066-1072.
- Hansen, J., G. Russell, D. Rind, P. Stone, A. Lacis, S. Lebedeff, R. Ruedy, and L. Travis, 1983: Efficient three-dimensional global models for climate studies: Models I and II. Mon. Wea. Rev., 111, 609-662.
- Henderson-Sellers, A., 1986: Layered cloud amounts for January and July, 1979 from 3-D Nephanalysis. J. Clim. Appl. Meteor., 25, 118-132.
- Heymsfield, A.J., 1972: Ice crystal terminal velocities. J. Atmos. Sci., 29, 1348-1357.
- Heymsfield, A.J., 1977: Precipitation development in stratiform ice clouds: A microphysical and dynamical study. J. Atmos. Sci., 34, 367-381.
- Heymsfield, A.J., and C.M.R. Platt, 1984: A parameterization of the particle size spectrum of ice clouds in terms of the ambient temperature and the ice water content. J. Atmos. Sci., 41, 846-856.
- Heymsfield, A.J., and L.J. Donner, 1990: A scheme for parameterizing ice-cloud water content in general circulation models. J. Atmos. Sci., 47, 1865-1877.
- Hughes, N.A., 1984: Global cloud climatologies. A historical review. J. Clim. Appl. Meteor., 23, 724-751.
- Koenig, G., K.N. Liou, and M. Griffin, 1987: An investigation of cloud radiation interactions using three-dimensional nephanalysis and earth radiation budget data bases. J. Geophys. Res., 92, 5540-5554.
- Koenig, L.R., 1971: Numerical modeling of ice deposition. J. Atmos. Sci., 28, 226-237.

- Koenig, L.R., and F. Murray, 1976: Ice-bearing cumulus cloud evolution: Numerical simulation and general comparison against observations. J. Appl. Meteor., 15, 747-762.
- Kyle, H.L., R.R. Hucek, B. Groveman, and R. Frey, 1990: Nimbus 7 ERB narrow field of view: Earth radiation budget projects. User's guide, Goddard Space Flight Center, Greenbelt, MD.
- Liou, K.N., and G.D. Wittman, 1979: Parameterization of the radiative properties of clouds. J. Atmos. Sci., 36, 1261-1273.
- Liou, K.N., and S.C. Ou, 1981: Parameterization of infrared radiative transfer in cloudy atmospheres. J. Atmos. Sci., 38, 2707-2716.
- Liou, K.N., and S.C. Ou, 1983: Theory of equilibrium temperatures in radiative-turbulent atmospheres. J. Atmos. Sci., 40, 214-229.
- Liou, K.N., and Q. Zheng, 1984: A numerical experiment on the interactions of radiation, clouds and dynamic processes in a general circulation model. J. Atmos. Sci., 41, 1513-1535.
- Liou, K.N., 1986: Influence of cirrus clouds on weather and climate processes: A global perspective. Mon. Wea. Rev., 114, 1167-1199.
- London, J., 1957: A study of the atmospheric heat balance. AFCRC-TR-57-287, College of Engineering, New York University, N.Y.
- Mason, B.J., 1971: The Physics of Clouds. 2nd Edition, Clarendon Press, 671 pp.
- Mitchell, J.F.B., C.A. Senior, and W.J. Ingram, 1989: CO₂ and climate: A missing feedback? Nature, 341, 132-134.
- Ou, S.C., and K.N. Liou, 1983: Parameterization of carbon dioxide 15 μ m absorption and emission. J. Geophys. Res., 88, 5203-5207.
- Ou, S.C., and K.N. Liou, 1988: Development of radiation and cloud parameterization programs for AFGL global models. Scientific Report, Air

Force Geophysics Laboratory, AFGL-TR-88-0018, 88 pp.

Prabhakara, C., I. Wang, A.T.C. Chang, and P. Gloersen, 1983: A statistical examination of Nimbus 7 SMMR data and remote sensing of sea surface temperature, liquid water content in the atmosphere and surface wind speed. J. Clim. Appl. Meteor., 22, 2033-2037.

Prabhakara, C., and D.A. Short, 1984: Nimbus-7 SMMR derived seasonal variations in the water vapor, liquid water and surface winds over the global oceans. NASA Technical Memorandum 86080, Goddard Space Flight Center, Greenbelt, Maryland, U.S.A.

Ramanathan, V., E.J. Pitcher, R.C. Malone, and M.L. Blackmon, 1983: The response of a spectral general circulation model to refinements in radiative processes. J. Atmos. Sci., 40, 605-630.

Roeckner, E., 1988: Cloud-radiation feedbacks in a climate model. Atmos. Res., 21, 293-303.

Slingo, J.M., 1987: The development and verification of a cloud prediction scheme for the ECMWF model. Quart. J. Roy. Meteor. Soc., 113, 899-927.

Slingo, A., and J.M. Slingo, 1988: The response of a general circulation model to cloud longwave radiative forcing. I: Introduction and initial experiments. Quart. J. Roy. Meteor. Soc., 114 1027-1062.

Smagorinsky, J., 1960: On the dynamical prediction of large-scale condensation by numerical methods. Monograph No. 5, Amer. Geophys. Union, 71-78.

Smith, R.N.B., 1990: A scheme for predicting layer clouds and their water content in a general circulation model. Quart. J. Roy. Meteor. Soc., 116, 435-460.

Starr, D.C., and S.K. Cox, 1985: Cirrus clouds. Part I: A cirrus cloud model. J. Atmos. Sci., 42, 2663-2681.

- Stephens, G.L., 1978: Radiative properties of extended water clouds. J. Atmos. Sci., 35, 2111-2132.
- Sundqvist, H., 1978: A parameterization scheme for non-convective condensation including prediction of cloud water content. Quart. J. Roy. Meteor. Soc., 104, 677-690.
- Sundqvist, H., 1981: Prediction of stratiform clouds: Results from a 5-day forecast with a global model. Tellus, 33, 242-253.
- Sundqvist, H., 1988: Parameterization of condensation and associated clouds in models for weather prediction and general circulation simulation. In Physically Based Modelling and Simulation of Climate and Climatic Change, M.E. Schlesinger (ed.), Reidel, Dordrecht, Part 1, 433-461.
- Washington, W.M., and D.L. Williamson, 1977: A description of the NCAR global circulation models, in Methods in Computational Physics. Vol. 17. General Circulation Models of the Atmosphere, edited by J. Chang, pp. 111-172, Academic Press, New York.
- Washington, W.M., and G.A. Meehl, 1984: Seasonal cycle experiment on the climate sensitivity due to a doubling of CO₂ with an atmospheric general circulation model coupled to a simple mixed-layer ocean model. J. Geophys. Res., 89, 9475-9503.
- Wetherald, R.T., and S. Manabe, 1988: Cloud feedback processes in a general circulation model. J. Atmos. Sci., 45, 1397-1415.
- Xu, K.M., and S.K. Krueger, 1991: Evaluation of cloudiness parameterizations using a cumulus ensemble model. Mon. Wea. Rev., 119, 342-367.
- Yang, G.H., K. Mitchell, D. Norquist, and S. Yee, 1989: Diagnostics for and evaluations of new parameterization schemes for global NWP models. GL-TR-89-0158. Environmental Research Papers Number 1032, Geophysics Laboratory, Atmospheric Sciences Division, Hanscom AF Base, MA 01731.

FIGURE CAPTIONS

- Figure 1. Empirical relations between the low-, middle-, and high-cloud amount and relative humidity (Smagorinsky, 1960). The values of h_0 for low, middle, and high clouds are 0.6, 0.35, and 0.26, respectively.
- Figure 2. Schematic display of the cloud microphysical processes simulated in the model.
- Figure 3. (a) Comparison of zonal-mean total cloudiness between 3DNEPH and model simulated results averaged over the time period, July 3-4; (b) Comparison of the zonally averaged OLR computed from the model and derived from ERB data. The model results and ERB data are averaged over the time period, July 3-4; (c) Comparison of the zonal mean LWP in the simulation and from SMMR data. The SMMR results are taken from Prabhakara and Short (1984) for the monthly average of June, 1979. Only the LWPs that are zonally averaged over the oceans are shown in the figure for both simulation and SMMR data.
- Figure 4. The geographical distribution of total cloud cover averaged over the period, July 3-4 (a) derived from 3DNEPH and (b) simulated by the model. The scale on the right of each figure shows the shading for the different cloud amount intervals. The brighter the cloud picture, the larger the cloud cover is.
- Figure 5. The geographical distribution of OLR averaged over the time period, July 3-4 in W/m (a) derived from ERB data and (b) simulated by the model. The scale on the right of each figure shows the shading for the different flux intervals.
- Figure 6. The geographical distribution of LWP in 10 g/m^2 (a) derived from SMMR data for the monthly average of July, 1979 (Prabhakara and

Short, 1984) and (b) simulated by the model for two days average covering July 3-4.

Figure 7. The model simulations for zonal-mean cloud IWC with a contour interval of $2.5 \times 10^{-3} \text{ g/m}^3$.

Figure 8. The model predicted zonal mean fields of (a) cloud cover, and (b) cloud LWC. The model results are averaged over the time period, July 3-4.

Figure 9. Zonally averaged differences in solar and IR radiative heating rates. The differences are obtained by subtracting the results in EXP1 from those in CTRL. The contour intervals for solar and IR heating rates are 0.5 and 2 K/day, respectively.

Figure 10. As in Fig. 9, but for differences in net heating rate and temperature.

Figure 11. As in Fig. 9, but for differences in cloud cover and total cloud water with contour intervals of 10% and $2 \times 10^{-3} \text{ g/m}^3$, respectively.

Figure 12. Zonally averaged differences in cloud LWC and total cloud water. The differences are obtained by subtracting the results in EXP2 from those in CTRL. The contour intervals for cloud LWC and total cloud water are $2 \times 10^{-3} \text{ g/m}$ and 10^{-3} g/m^3 , respectively.

Figure 13. Zonally averaged differences in (a) cloud LWC, (b) cloud IWC, and (c) total cloud water. The differences are obtained by subtracting the results without ice phase from those with ice phase in the case of a small autoconversion rate. The contour intervals for cloud LWC and total cloud water are $2 \times 10^{-3} \text{ g/m}^3$ and 10^{-3} g/m^3 , respectively.

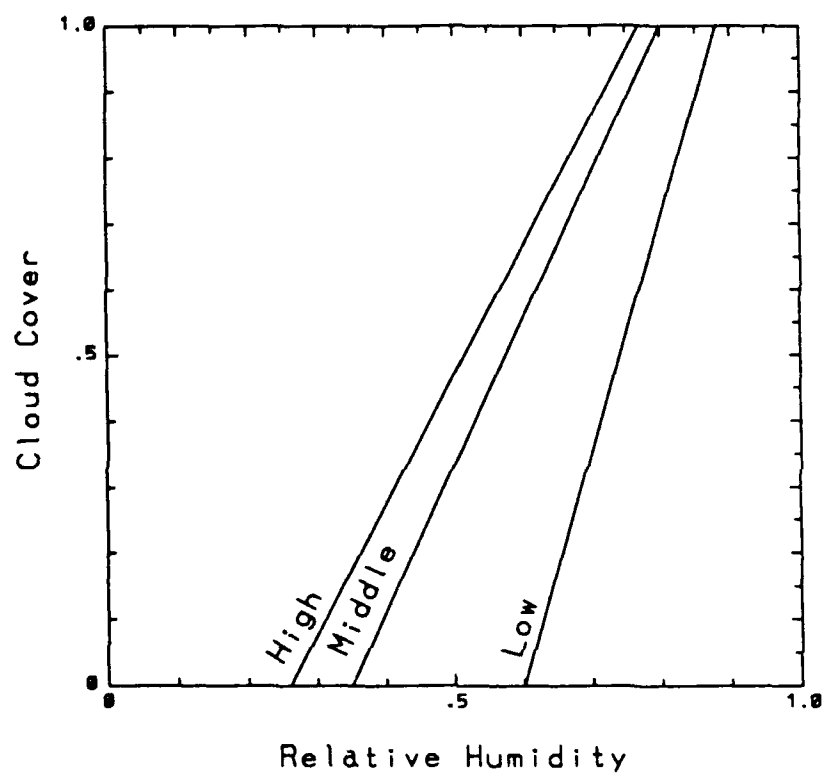


Fig. 1

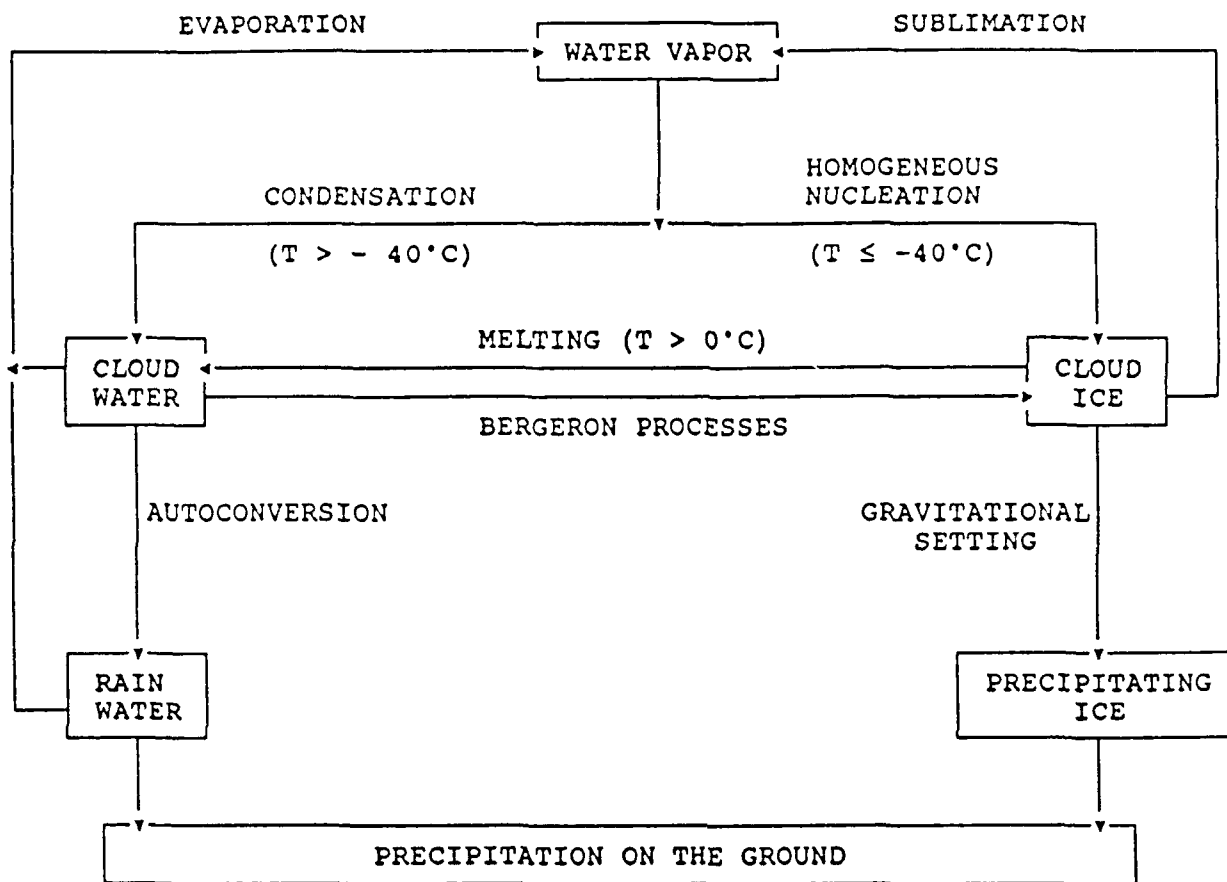


Fig. 2

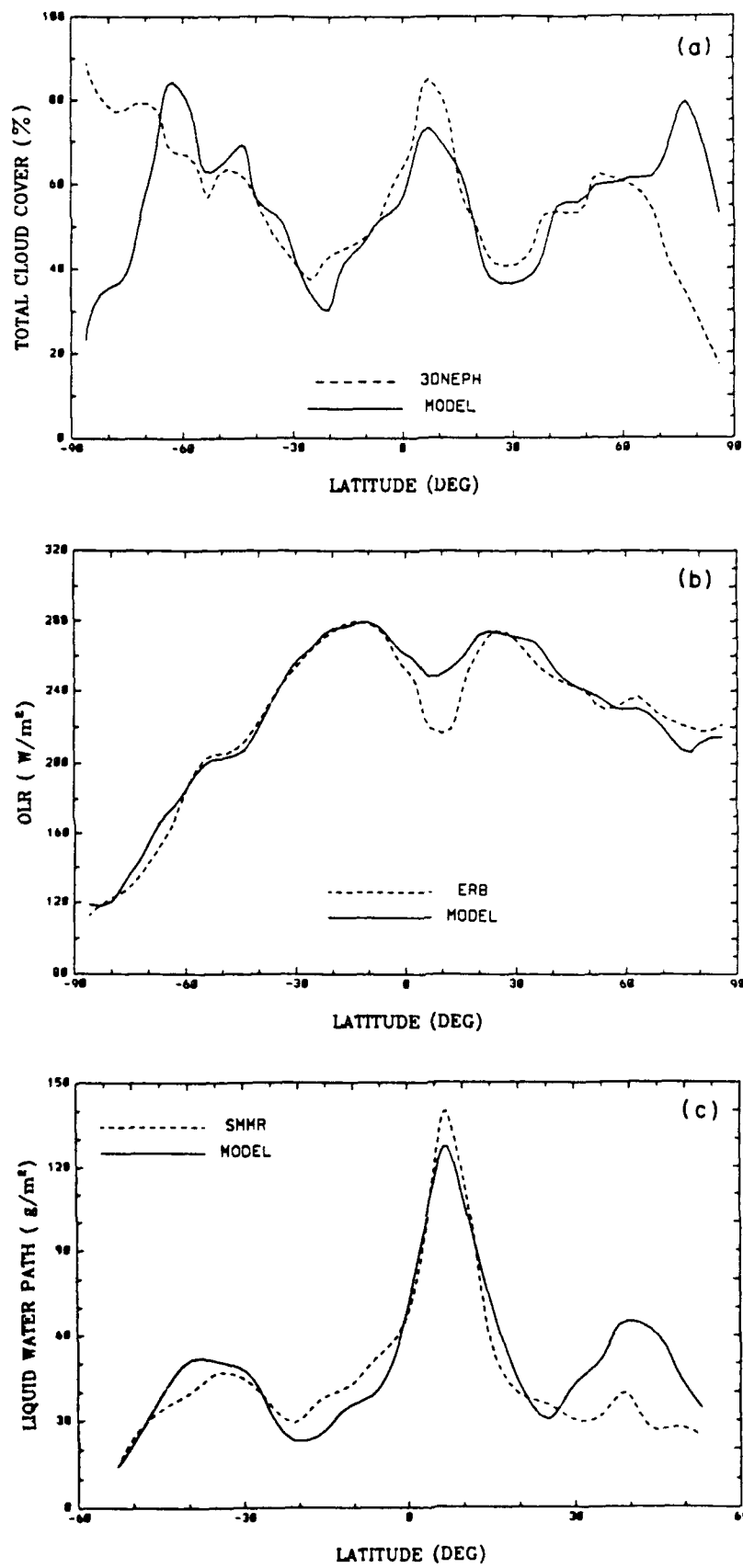


Fig. 3

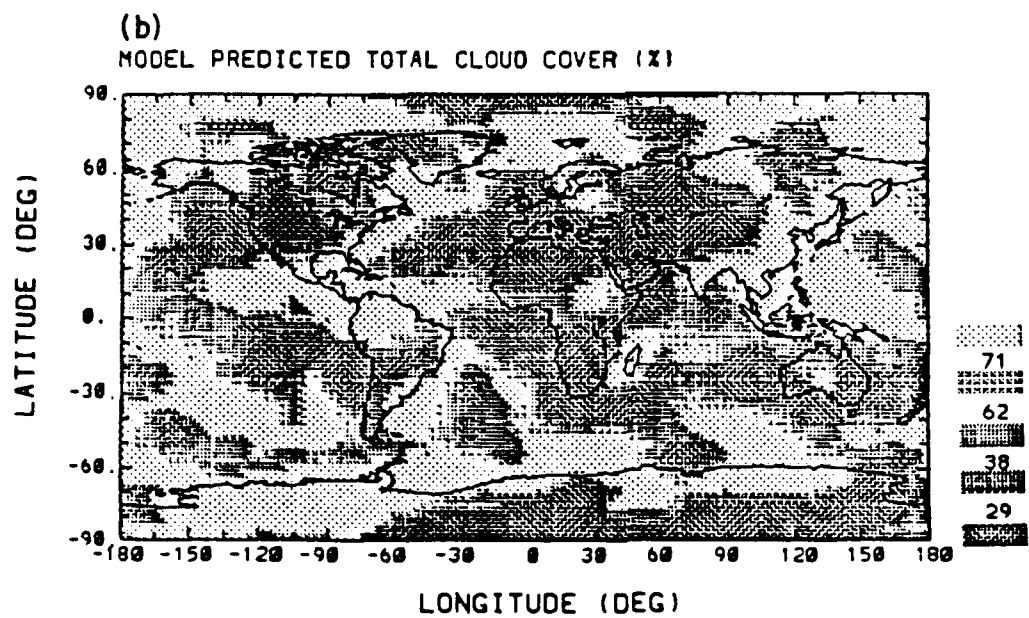
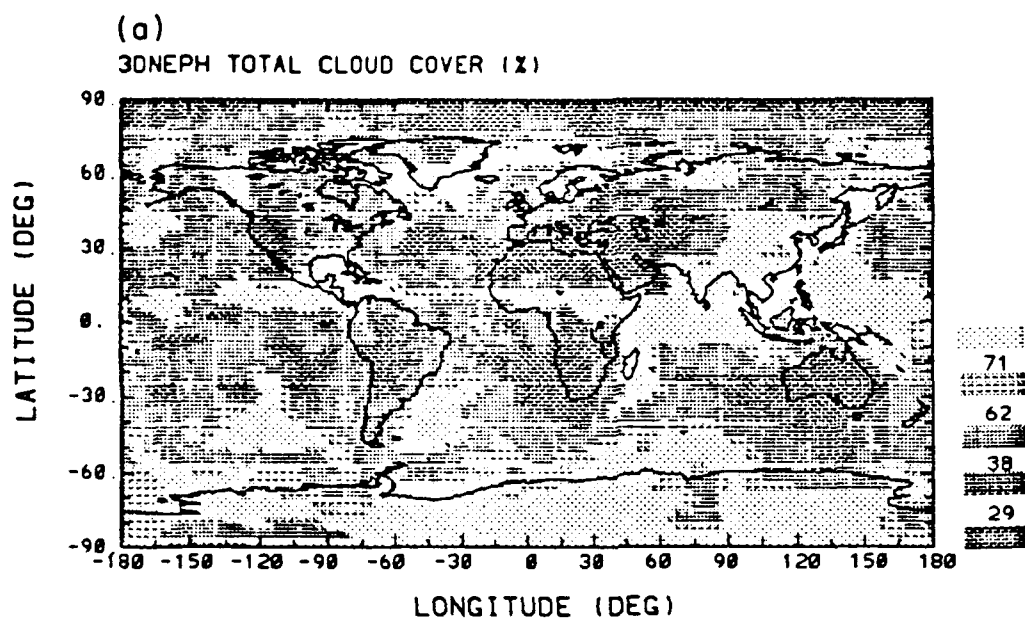


Fig. 4

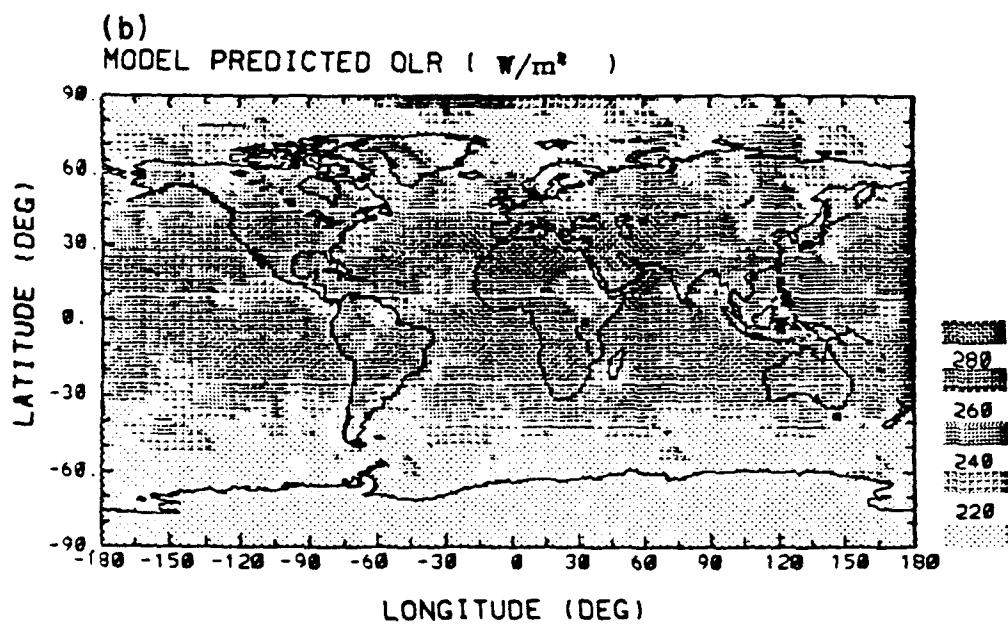
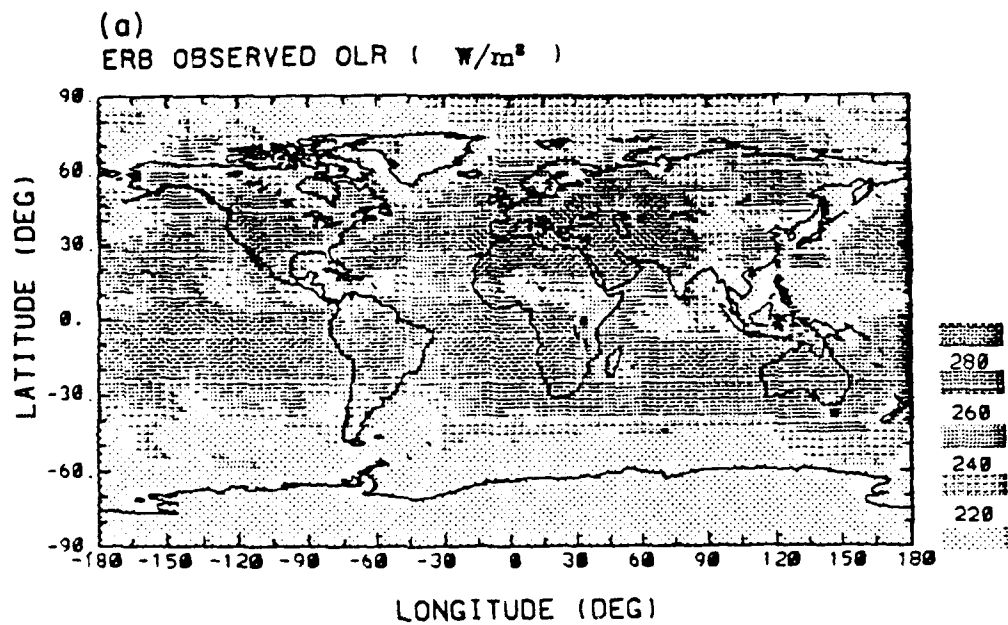


Fig. 5

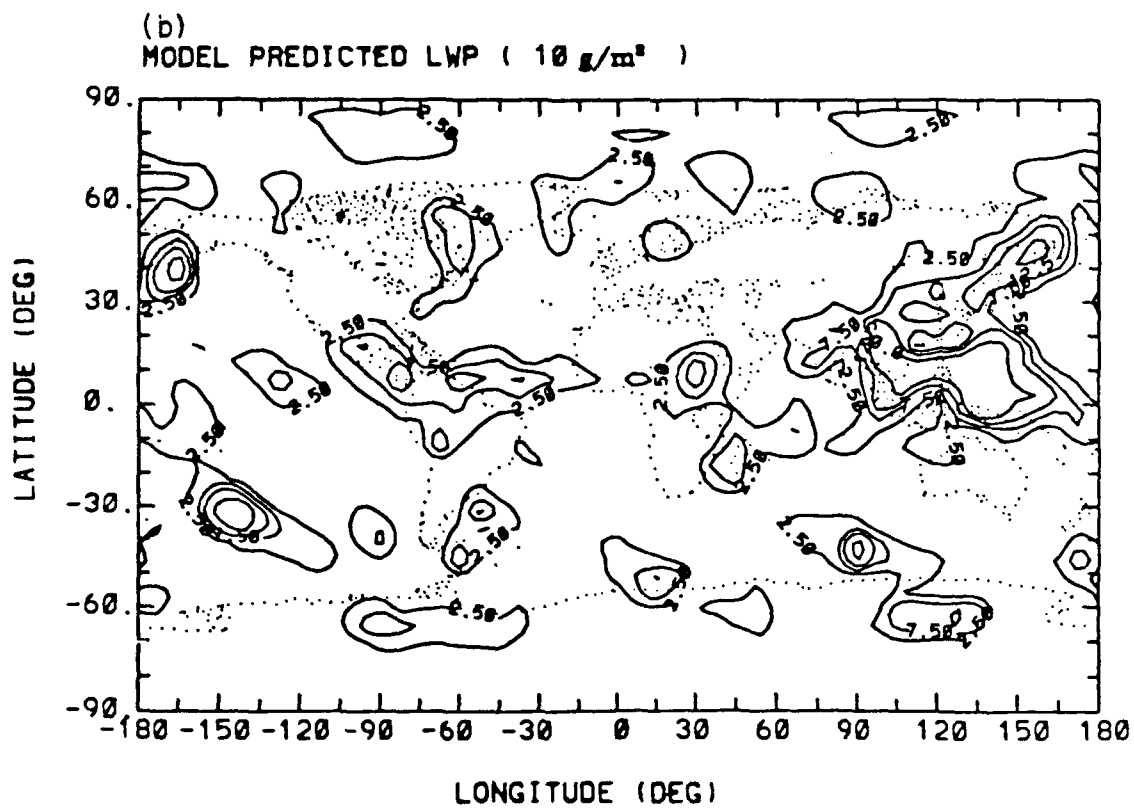
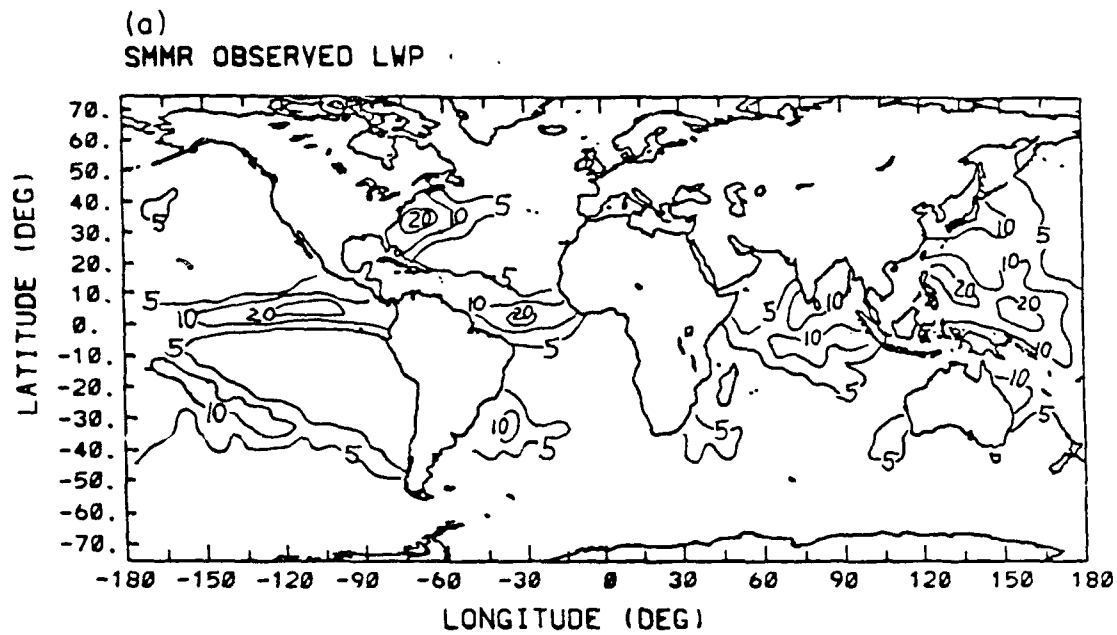


Fig. 6

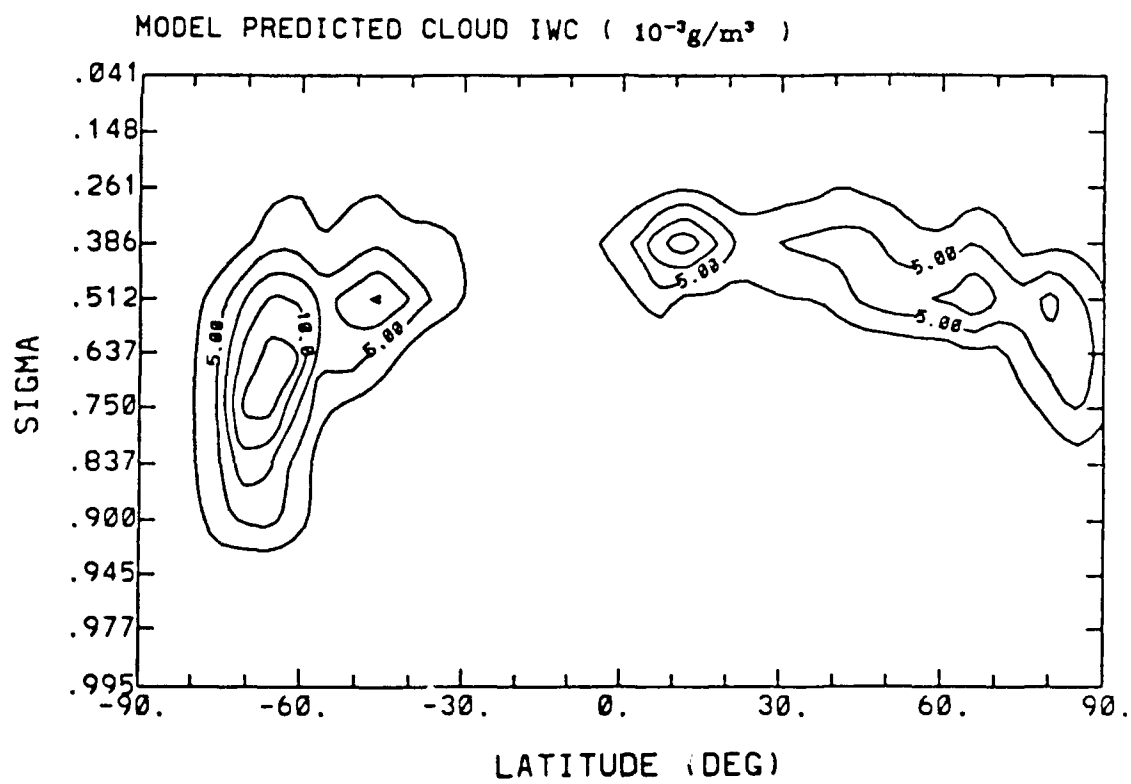
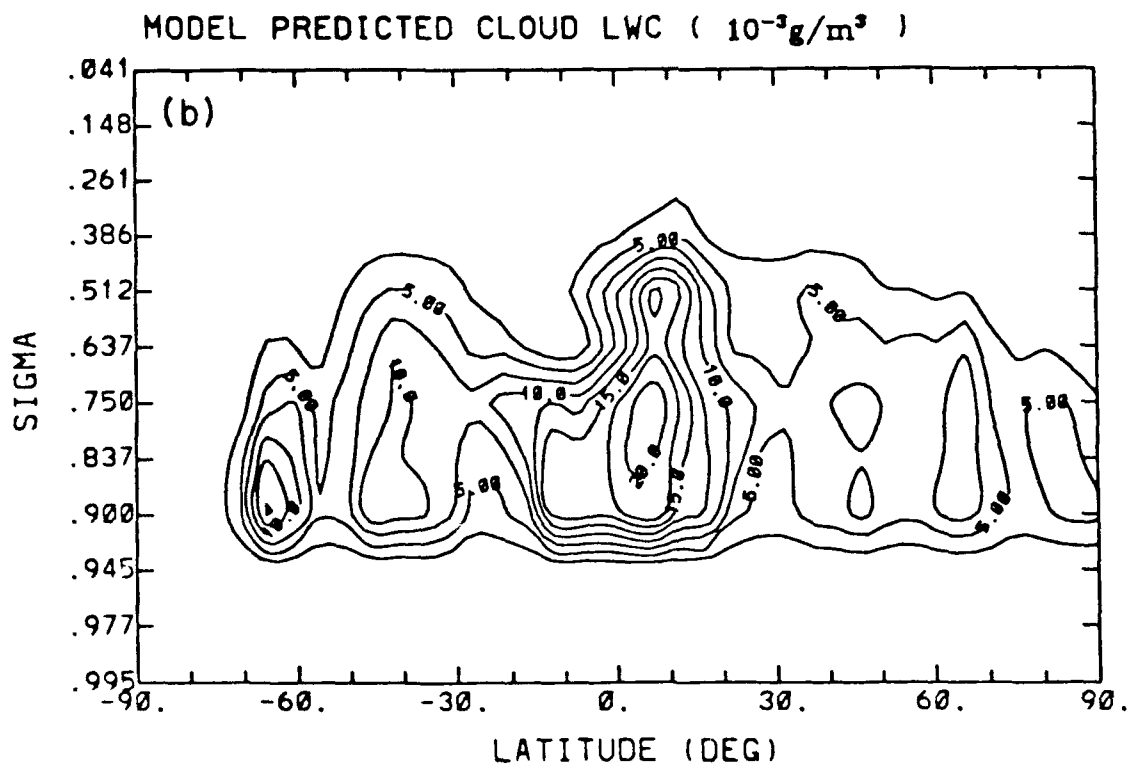
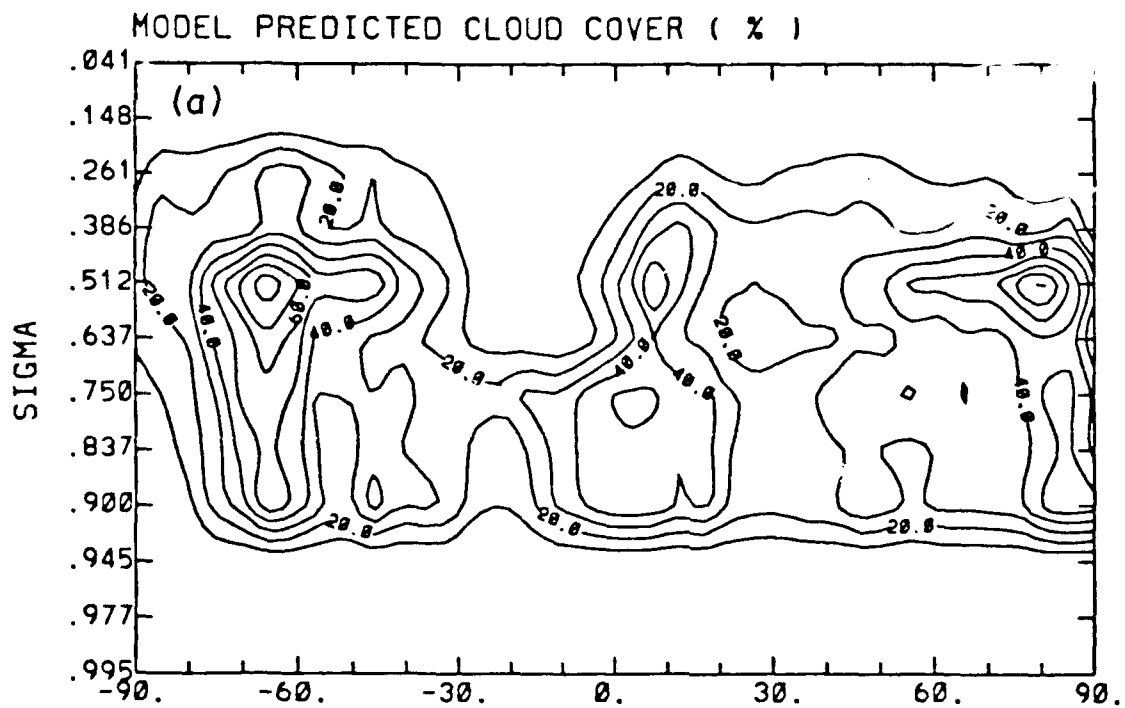


Fig. 7



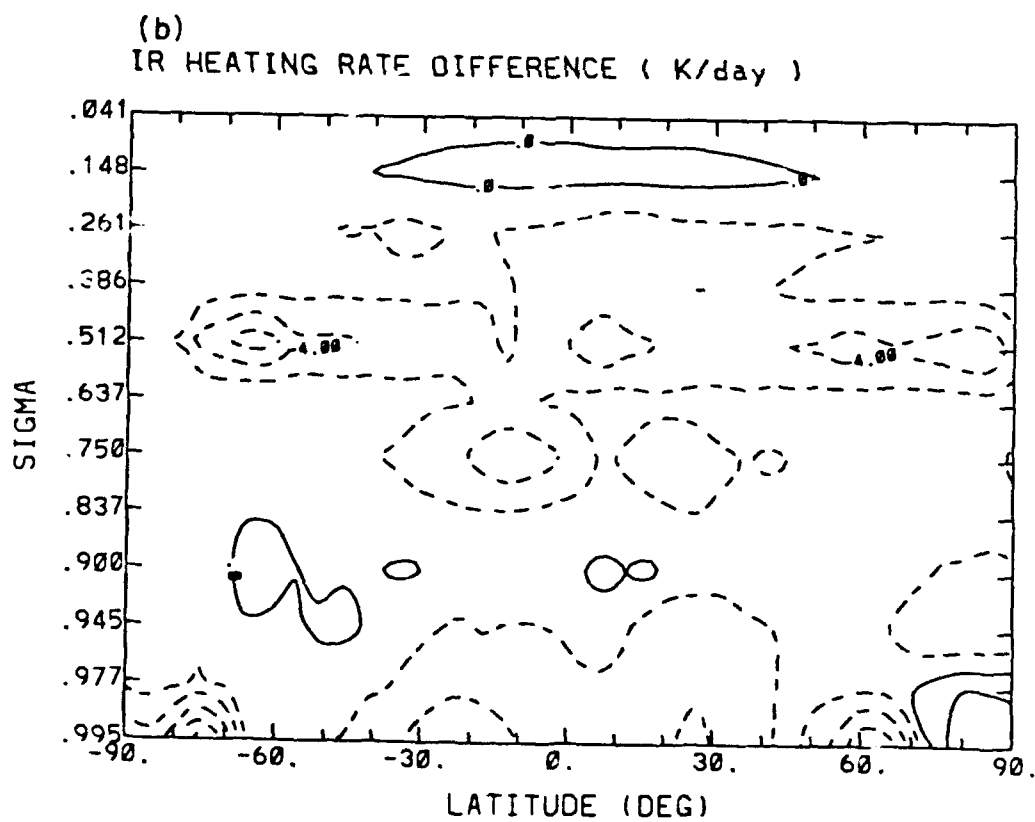
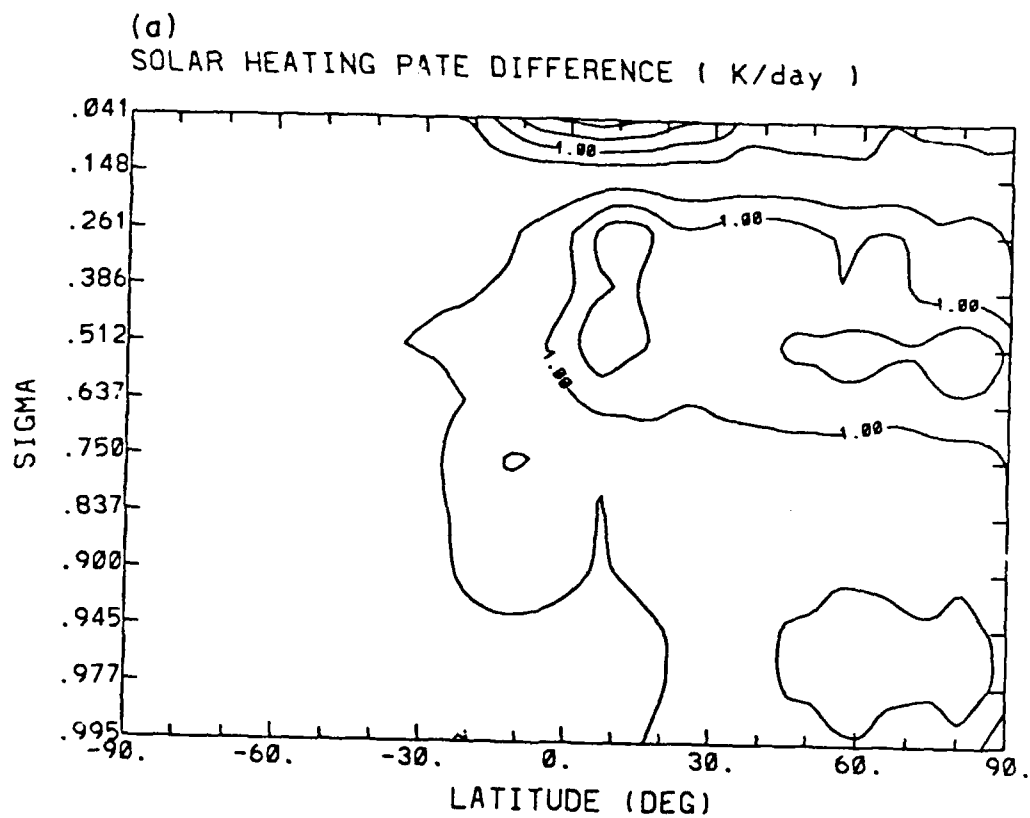


Fig. 9

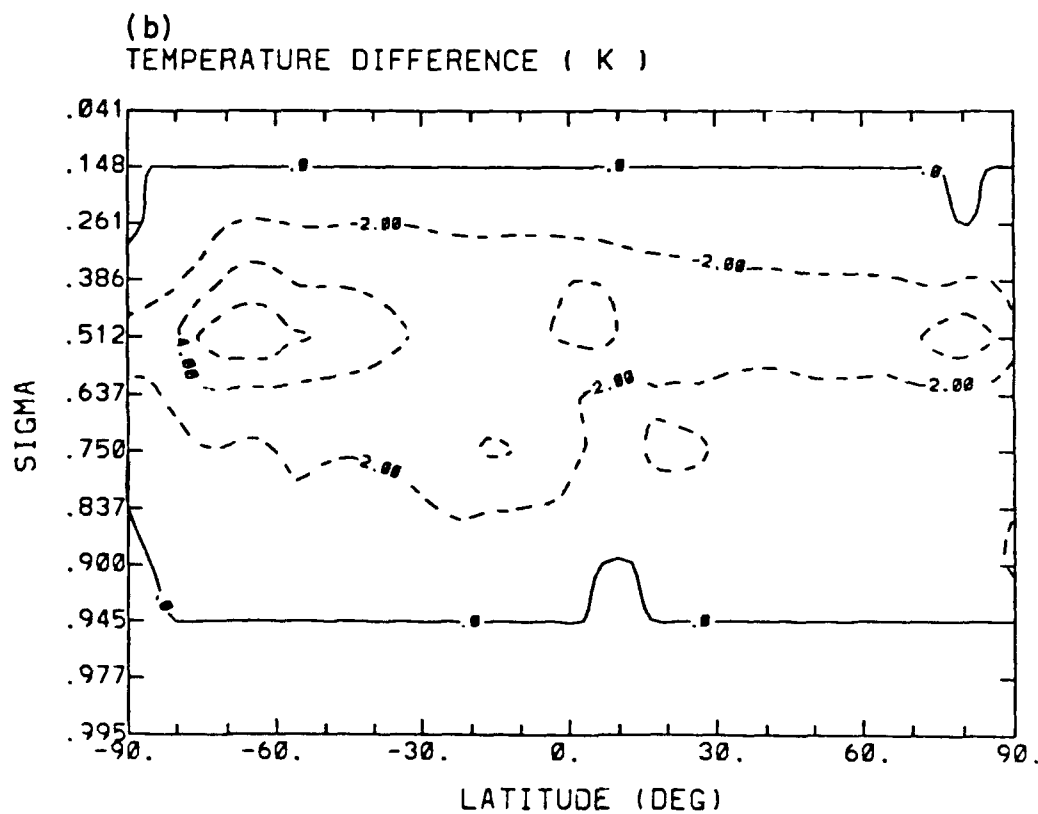
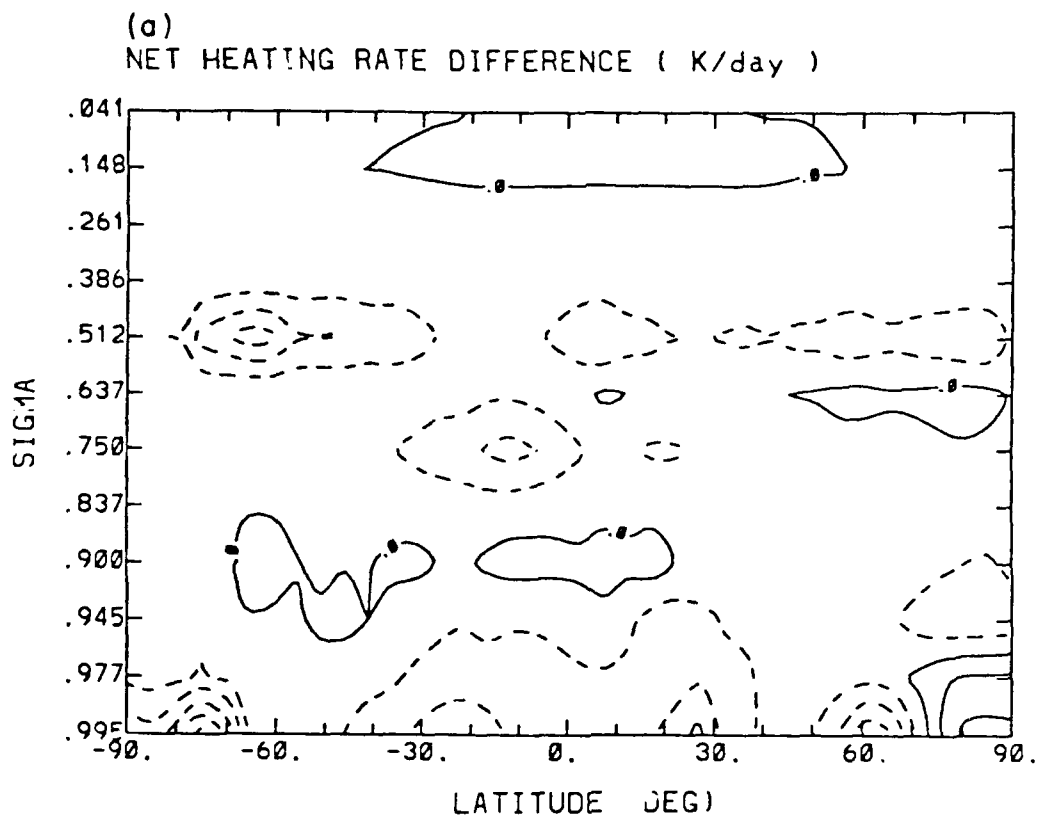


Fig. 10

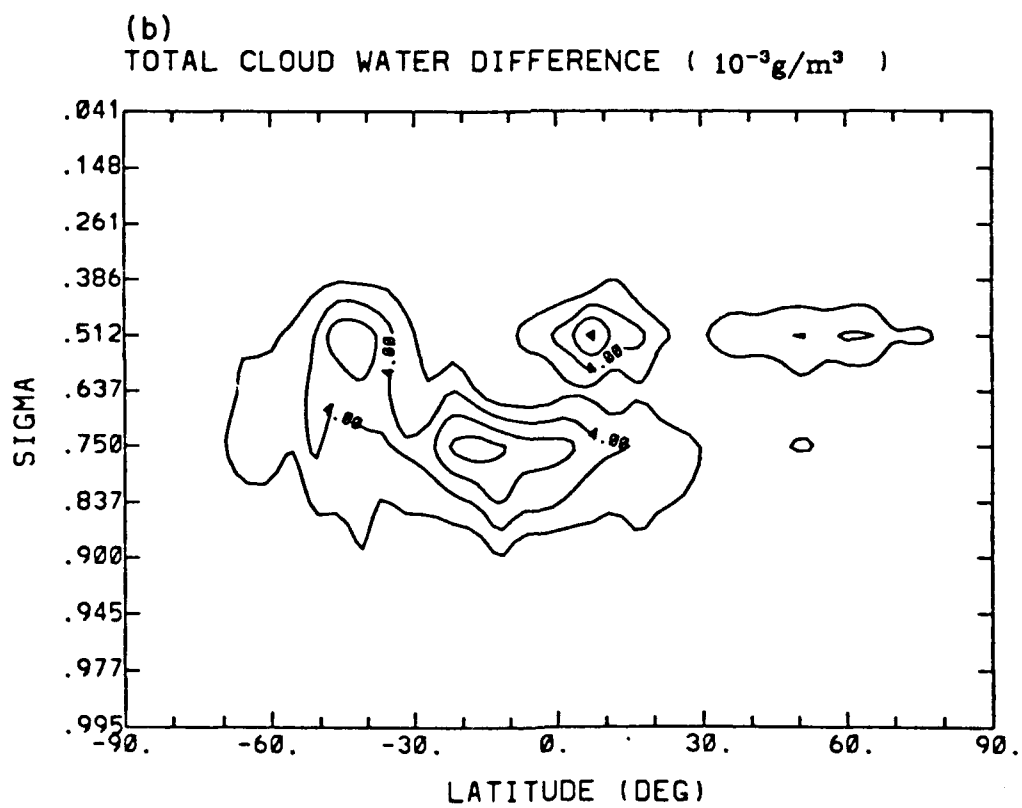
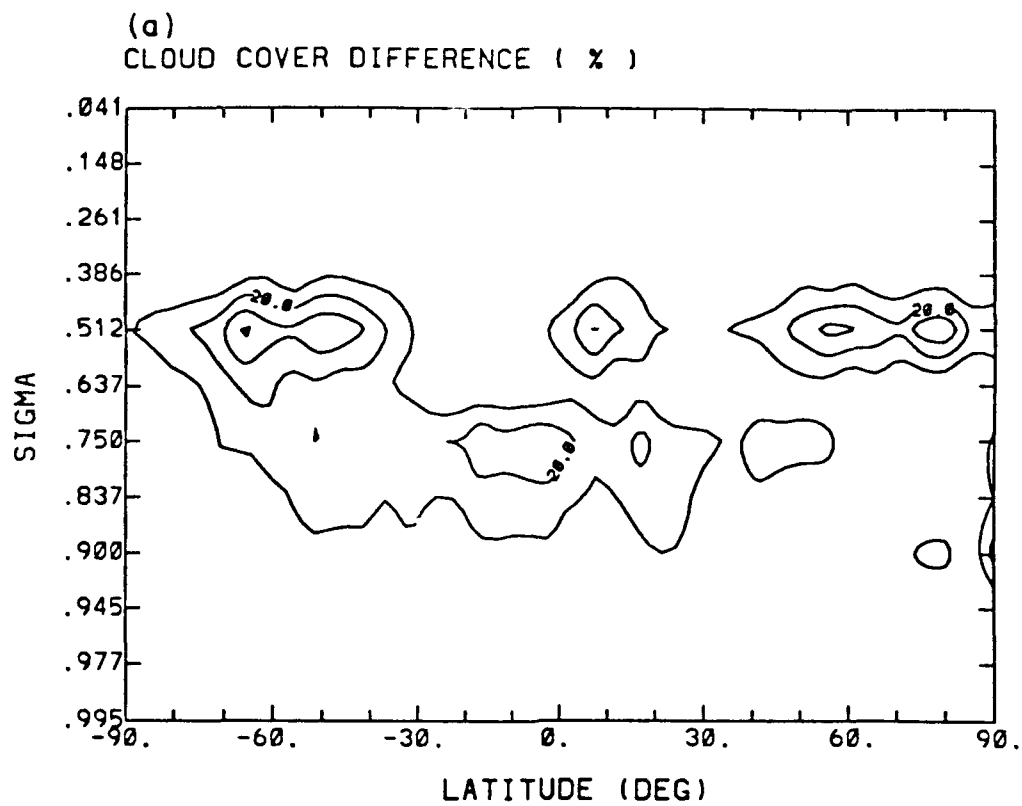


Fig. 11

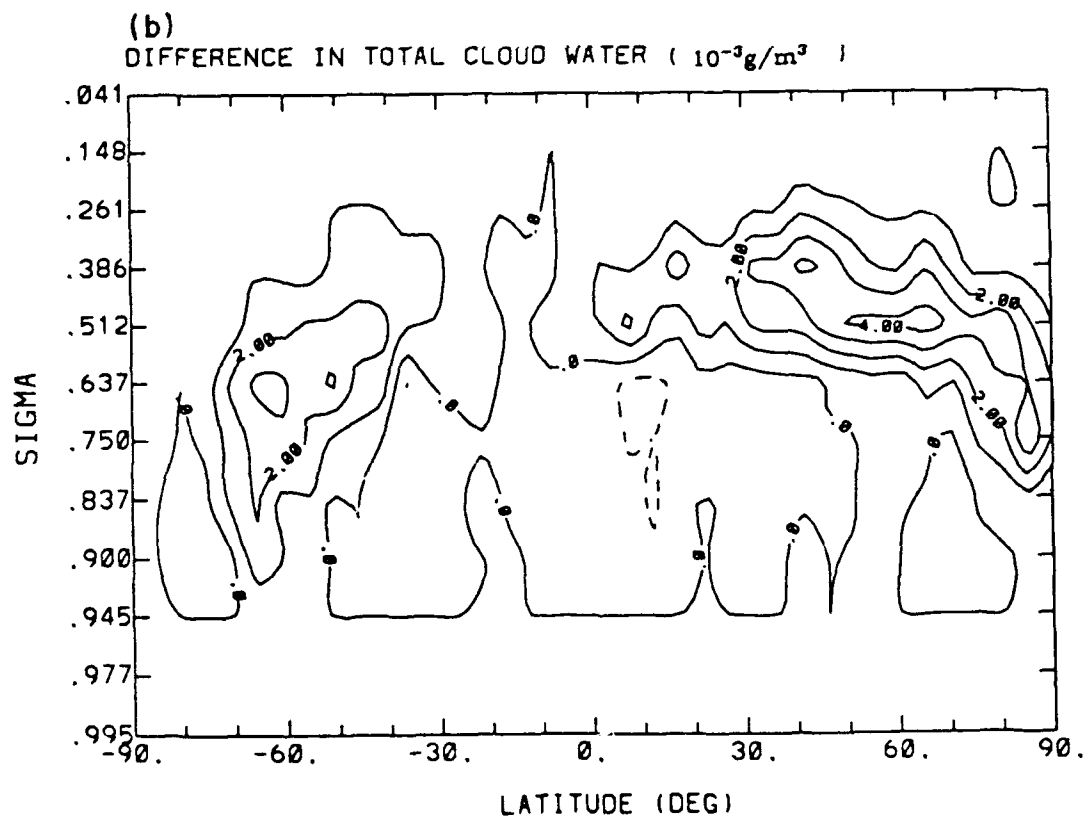
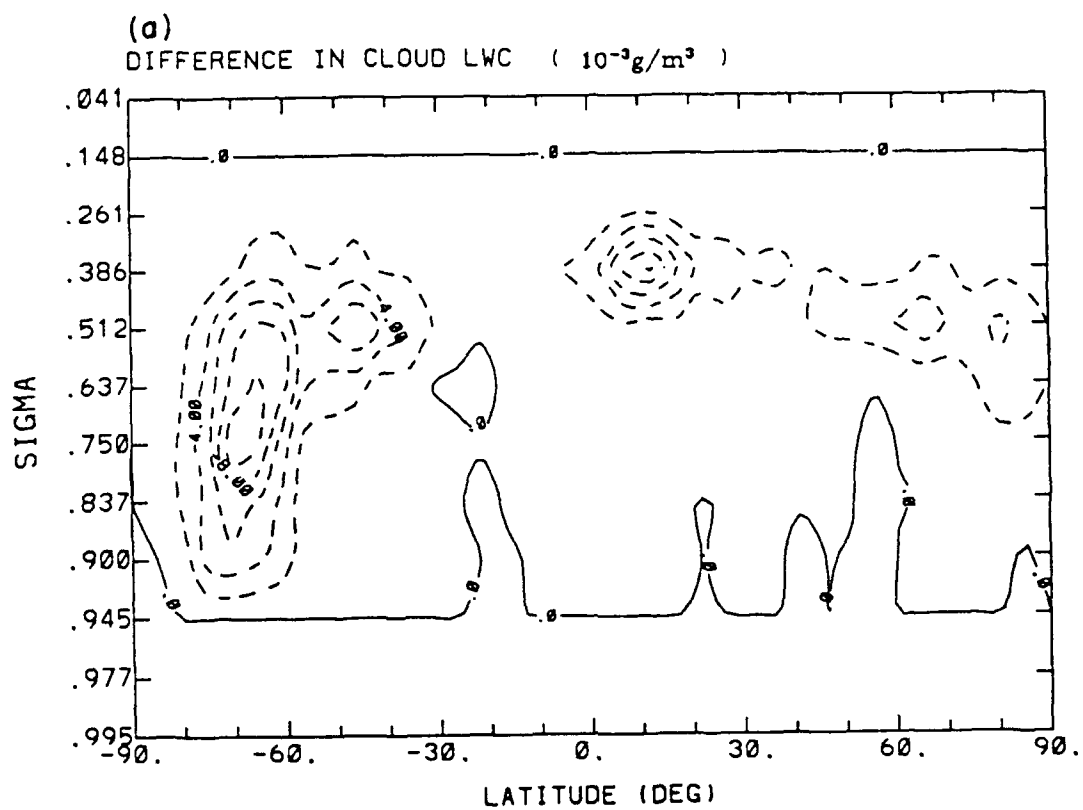


Fig. 12

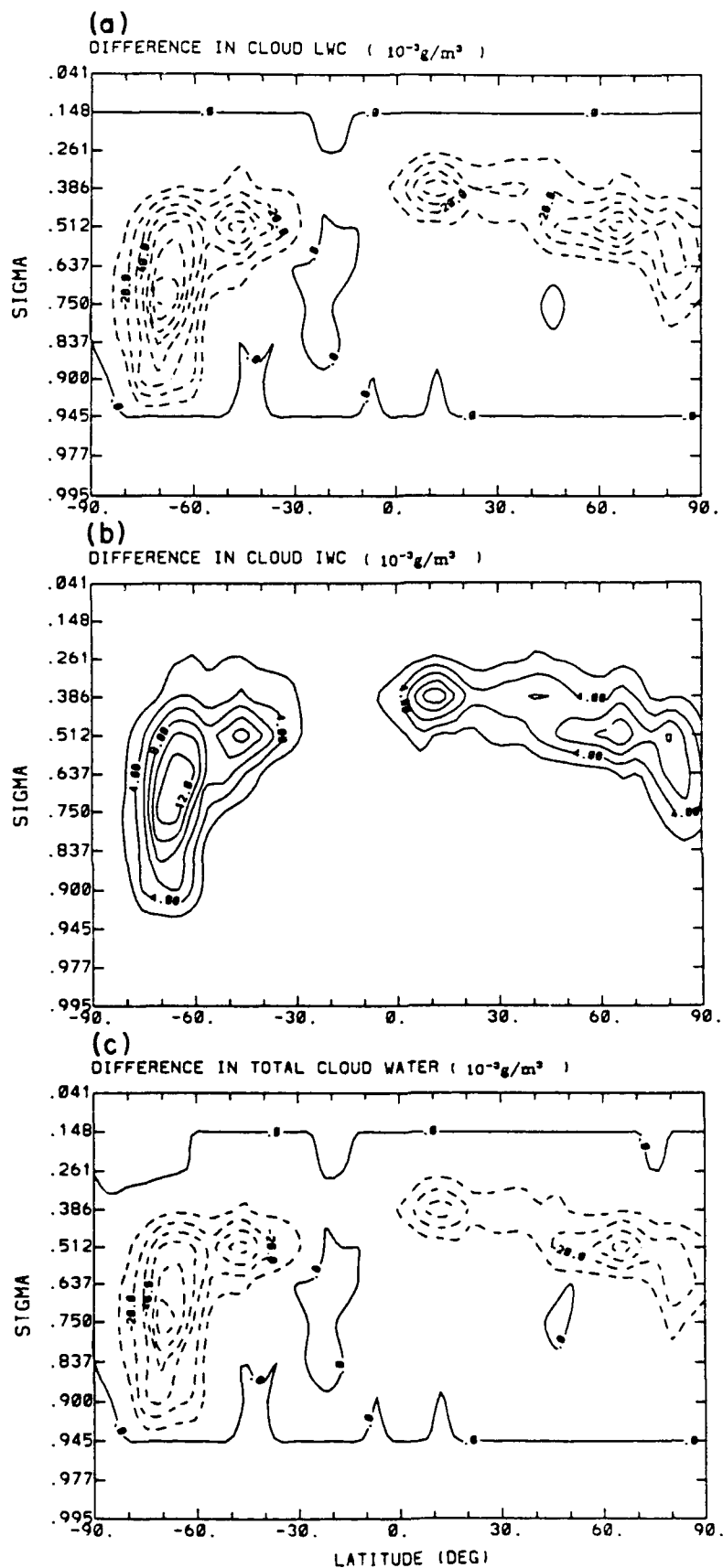


Fig. 13

University of Utah, Department of Meteorology CARSS, Salt Lake City, Utah 84112, U.S.A.

Ice Cloud Microphysics, Radiative Transfer and Large-Scale Cloud Processes

K. N. Liou, J. L. Lee, S. C. Ou, Q. Fu and Y. Takano

With 7 Figures

Received September 7, 1990

Revised January 31, 1991

Summary

Parameterization programs for cloud microphysics and radiative transfer involving ice clouds have been developed in terms of the mean effective size and ice water path. The mean effective size appears to be adequate in representing the ice crystal size distribution for radiative parameterizations. For a given ice water path, smaller mean effective sizes reflect more solar radiation, emit more IR radiation and enhance net radiative heating/cooling at the cloud top and bottom than larger sizes. The presence of small ice crystals may generate steeper lapse rates in clouds. A 3-D global cloud model that prescribes the horizontal wind fields in a 24 hour period is used to investigate the sensitivity of the mean effective size of ice crystals on the simulation of radiative heating, temperature, cloud cover and ice water content. A variation in the mean effective size from 75 to 50 μm in a 24 hour prediction simulation generates more cooling above the high cloud top and a decrease of temperature. These results lead to an increase of high cloud cover in some latitudes by as much as 4% and, at the same time, a decrease of middle cloud cover by 3–4% in latitudes between 60°S and 60°N.

1. Introduction

In recognition of the importance of the role of clouds in weather and climate processes, numerous efforts have been made to include a more realistic and physically based parameterization for cloud parameters in general circulation models (Sundqvist, 1988; Liou and Zheng, 1984; Heymsfield and Donner, 1990; Smith, 1990). To understand the effects and feedbacks of clouds on dynamic and

thermodynamic systems, the microphysical processes that govern the formation and dissipation of clouds must be adequately incorporated in atmospheric models. Furthermore, the radiative properties of clouds are determined by the cloud thermodynamic phase (ice or water), particle size distribution and geometric configuration. It appears to be impractical to include individual cloud particles in cloud models and radiation calculations. We must rely on some aspect of the cloud particle size distribution in the performance of radiation parameterizations in numerical models.

In this paper, we explore the means by which cloud microphysics and radiative transfer can be effectively and physically parameterized for incorporation in large-scale cloud and atmospheric models. We shall confine our presentation to high clouds that contain ice particles. In Sections 2 and 3, we present parameterization programs for cloud microphysics and radiative transfer in clouds, respectively. The mean effective size is proposed to represent ice crystal size distribution in radiation parameterizations. In Section 4, we investigate the sensitivity of mean effective size to the simulation of radiative heating, temperature, cloud cover and ice water content (IWC) using the global cloud model developed by Lee et al. (1990). Finally, conclusions are given in Section 5.

2. Parameterization of Cloud Microphysics

It is not computationally feasible to account for individual cloud particles in radiative transfer calculations. Nor is it practical to incorporate a program that takes into account the growth of individual water droplets and ice crystals in cloud models. However, some measure of the particle size distribution may be used. From the perspective of radiation calculations, particles scatter an amount of light proportionate to their cross-section area. The cross-section of a nonspherical particle is proportional to the maximum dimension (or the length, L) multiplied by the width, D . Thus, we may define a mean effective width (size) for hexagonal ice crystals in the form

$$D_e = \frac{\int_{L_{\min}}^{L_{\max}} D \cdot L D n(L) dL}{\int_{L_{\min}}^{L_{\max}} L D n(L) dL}, \quad (1)$$

where L_{\min} and L_{\max} denote the limits of the ice crystal length. From laboratory and aircraft observations (Auer and Veal, 1970; Heymsfield, 1972; Hobb et al., 1974), the width of an ice particle can be related to the length via the following equation: $D = a_1 L^{b_1}$, where a_1 and b_1 are certain coefficients that are dependent on the particle shape.

The ice water content is defined by

$$\text{IWC} = \int_{L_{\min}}^{L_{\max}} m(L) n(L) dL, \quad (2)$$

where the mass of an individual ice crystal may be related to the length (Heymsfield, 1972): $m = a_2 L^{b_2}$, with a_2 and b_2 being certain coefficients. From Eqs. (1) and (2), IWC and D_e may be related through the ice crystal size distribution. The vertical IWC or ice water path (IWP) for a given thickness, Δz , is

$$\text{IWP} = \text{IWC} \cdot \Delta z. \quad (3)$$

The other cloud physics parameter that is critically dependent on ice crystal size distribution is the bulk terminal velocity, which is defined by

$$V_T = \frac{\int_{L_{\min}}^{L_{\max}} n(L) m(L) v(L) dL}{\int_{L_{\min}}^{L_{\max}} n(L) m(L) dL}, \quad (4)$$

where v is the terminal velocity for an individual ice crystal, which can be determined by the crystal length based on laboratory results (Jayaweera and Cottis, 1969; Heymsfield 1972). Thus we have: $v = a_3 L^{b_3}$, with a_3 and b_3 being certain coefficients (Starr and Cox, 1985).

The ice crystal size distribution for midlatitude cirrus clouds has been measured by Heymsfield (1977) using an optical probe. Based on the measured data, Heymsfield and Platt (1984) grouped the size distributions according to temperatures ranging from -20 to -60°C and proposed a parameterized equation in the form

$$n(L) = A L^B, \quad (5)$$

where both coefficients A and B are dependent on temperature. The minimum length that an optical probe can measure is about $20\mu\text{m}$. It is probable that ice crystals smaller than $20\mu\text{m}$ could be missed by this measurement technique.

In view of the preceding discussion, the ice crystal width, mass, terminal velocity and size distribution may be parameterized in terms of the length. Using $D_{\min} = 20\mu\text{m}$, the bulk terminal velocity and mean effective width can be expressed as a function of the IWC, as shown in Fig. 1. In the calculations, we use a temperature range of $(-30 - -35^\circ\text{C})$ to obtain the coefficients A and B . Both D_e and v_T increase with increasing IWC. To investigate the effect of small ice crystals on these relationships, L_{\min} in Eq. (1) is set at $10\mu\text{m}$ and it is assumed that Eq. (4) is valid for the ice crystal size distribution that includes small ice crystals with sizes from 10 to $20\mu\text{m}$. The bulk terminal velocity ranges from about 1 to 10m/s for the

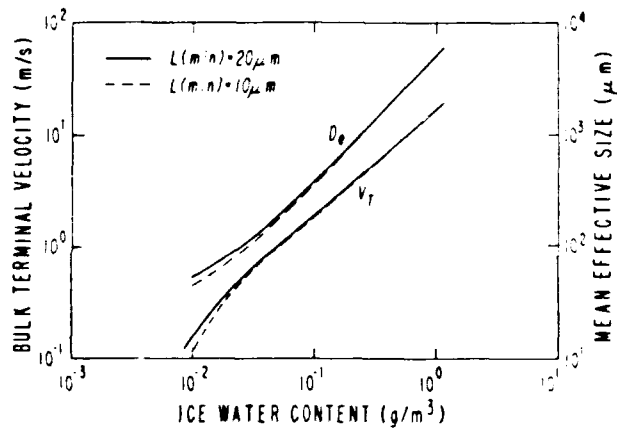


Fig. 1. Terminal velocity and mean effective size as functions of IWC

IWC from 0.1 to 1 g m⁻³. For IWCs smaller than 0.1 g m⁻³, the bulk terminal velocity is less than 1 m s⁻¹. The addition of ice crystals smaller than 20 μm does not affect the bulk terminal velocity significantly. Based on our present parameterizations for cloud microphysics, the mean effective size can also be theoretically computed in terms of IWC. For IWCs larger than 0.1 g m⁻³, the addition of 10–20 μm sized ice crystals results in no noticeable changes in mean effective sizes. For an IWC of 0.01 g m⁻³, the computed mean effective size is about 50 μm. With additional small ice crystals, this size reduces to about 40 μm. It should be emphasized that the relationship between the mean effective size and IWC that has been developed is purely theoretical and requires verification from laboratory and aircraft experiments.

Light scattering and absorption calculations require the ice crystal size distribution. However, for radiative heating and flux calculations, additional information concerning the cloud thickness and IWC is needed. It is conventional to use the optical depth to represent the optical properties of a media. The optical depth, τ , is the product of the extinction coefficient and thickness. The extinction coefficient is the product of the average extinction cross section, σ_e , and the number density of cloud particles. In the limits of geometric optics, and assuming that ice crystals are randomly oriented in space, we have $\sigma_e = 3D(\sqrt{3}/4D + L)/2$ (Takano and Liou, 1989a). This expression is derived based on the optical theorem that the extinction cross section of a large particle is twice its geometric cross section. In this case we find

$$\tau \cong (a + b D_e) \cdot \text{IWP}, \quad (6)$$

where a and b are certain constants. For radiative transfer calculations associated with a cloud model, the two parameters defined in Eqs. (1) and (2) appear to be appropriate and sufficient.

3. Parameterization of Radiative Transfer in Clouds

For the computations of fluxes and heating rates within cloud layers, we must perform spectral integration covering the entire solar and IR spectra. These spectra may be divided into a number of spectral intervals according to the location of the gaseous absorption bands involving cloud particles and gases, primarily water vapor. In order to resolve the variation in the refractive index of ice

and to account for the gaseous absorption, six and 12 bands are selected for solar and thermal IR regions, respectively. The radiative transfer methodology used is the delta-four-stream approximation developed by Liou et al. (1988). This approximation can achieve relative accuracy within about 5% for all atmospheric conditions. The solution of this approximation is in analytic form so that the computer time involved is minimal, and the method can be readily applied to inhomogeneous media by matching the continuity requirement of diffuse intensities. To apply this approximation, four expansion coefficients of the phase function are required.

The scattering and absorption properties of hexagonal ice crystals whose size parameters are greater than 30 were computed from the geometric ray-tracing technique developed by Takano and Liou (1989a, b). For size parameters that are less than 30, we used the Mie-type solution for spheroids developed by Asano and Sato (1980). Single-scattering computations were made for a number of ice crystal size distributions reported by Heymsfield and Platt (1984) and recently derived from the FIRE cirrus experiments (Heymsfield, private communication).

As pointed out previously, the optical depth may be expressed in terms of D_e and IWP, in the form given in Eq. (6), in the limits of geometric optics for scattering processes. The following general parameterization form has been derived for the spectral optical depth:

$$\tau_j = \left(\sum_{n=0}^2 a_n D_e^n \right) \cdot \text{IWP}, \quad (7)$$

where a_n is the known coefficient, and the subscript j ($= 1, 2, \dots, 18$) is the index for the spectral band. For solar wavelengths, the extinction cross sections would be the same by virtue of the geometric optical theorem. Thus, for a given thickness, Δz , the optical depth is a constant in the solar region based on the geometric ray tracing method for hexagonal ice crystals.

The single-scattering albedo is defined as: $\tilde{\omega} = 1 - \sigma_a/\sigma_e$, where σ_a and σ_e represent the absorption and extinction cross sections, respectively. In the limits of geometric optics, we have $\sigma_e = 3(D/2)^2(\sqrt{3}/4 + L/D)$, as pointed out previously. The absorption cross section is generally dependent on particle volume, which is: $V = 3\sqrt{3}D^2L/8$ in the

case of a hexagonal particle. Since L is related to D based on laboratory and aircraft observations, $\bar{\omega}$ should be a function of D . Thus, it is appropriate to represent $\bar{\omega}$ in terms of a polynomial function in the form

$$\bar{\omega}_j = \sum_{n=0}^3 b_n D_e^n, \quad (8)$$

where b_n is the known coefficient through numerical fittings. The third order polynomial is accurate within about 3%.

The phase function should also be a function of ice crystal size distribution, viz., the mean effective size. It follows that the expansion coefficients of the phase function may be written

$$\bar{\omega}_{l,j} = \sum_{n=0}^3 c_{n,l,j} D_e^n, \quad (9)$$

where the index $l = 1, 2, 3, 4$ for the delta-four-stream approximation, $\bar{\omega}_1 = 3g$, and g is the asymmetry factor. Again, we find that the third order polynomial expansion is sufficient to provide accuracy within 3%. For solar wavelengths, the phase functions for hexagonal ice crystals show pronounced 22 and 46° halo maxima. For this reason, a simple representation using the asymmetry factor for the transfer of solar radiation in ice clouds is inadequate. However, in the thermal IR wavelengths, halo features are largely suppressed due to absorption. Thus, we may use the asymmetry factor to represent the phase function through the Henyey-Greenstein function:

$$\bar{\omega}_l = (2l + 1)g^l. \quad (10)$$

Finally, to incorporate the forward peak contribution in multiple scattering, we may use the similarity principle for radiative transfer to adjust the optical depth, single-scattering albedo and phase function in the forms (Liou et al., 1988)

$$\tau' = \tau(1 - f\bar{\omega}), \quad (11a)$$

$$\bar{\omega}' = (1 - f)\bar{\omega}(1 - f\bar{\omega}), \quad (11b)$$

$$\bar{\omega}'_l = [\bar{\omega}_l - f(2l + 1)](1 - f), \quad (11c)$$

where the fraction of scattered energy residing in the forward peak, $f = \bar{\omega}_4/4$. The wavelength index j has been omitted in these equations.

Using the preceding parameterizations for cloud physics and radiative transfer, Fig. 2 shows solar reflectance and absorptance and IR emittance

(or emissivity) as functions of D_e and IWP. A cosine of the solar zenith angle of 0.5 is used in solar radiative transfer calculations. For a given D_e , solar reflectance increases with increasing IWP. But for a given IWP, a cloud with a smaller D_e reflects more solar radiation because of the larger effective cross section area. For example, for an IWP of 100 g m^{-2} , solar reflectances of

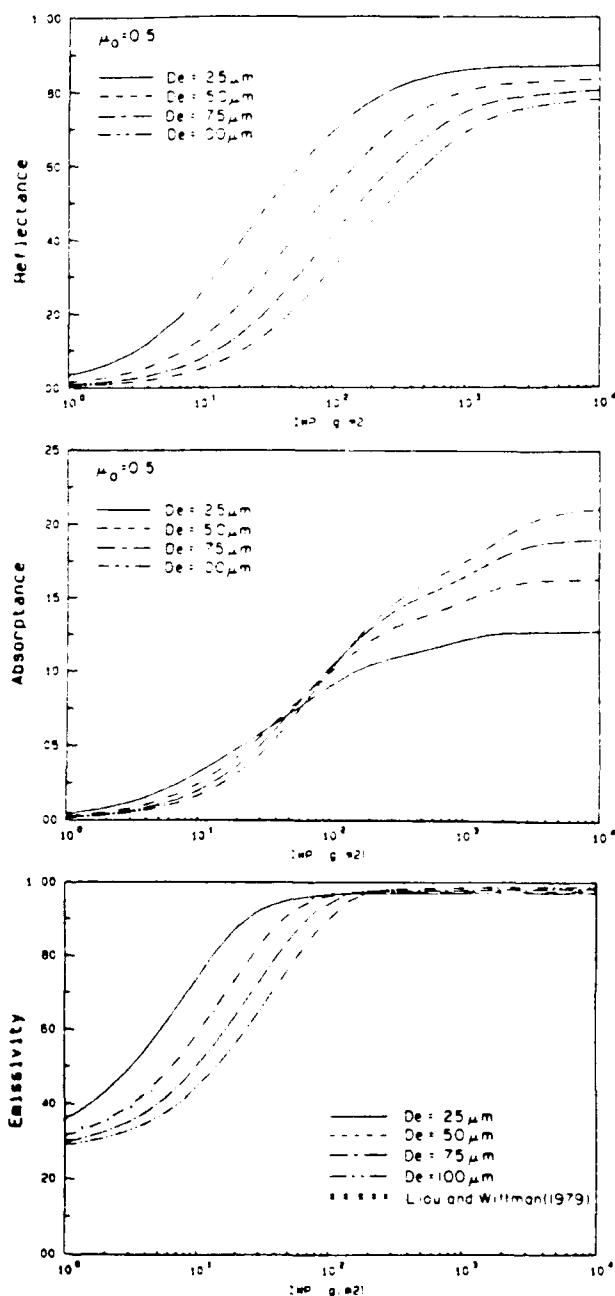


Fig. 2 Solar reflectance and absorptance and IR emittance (or emissivity) as functions of the mean effective size and ice water path

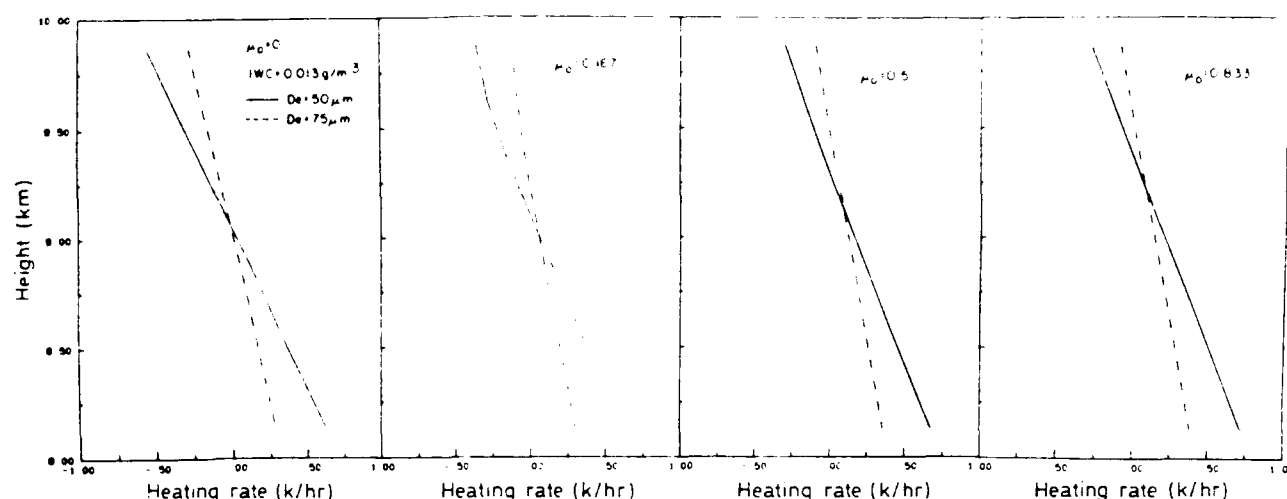


Fig. 3. Net radiative heating rates as functions of height and cosines of the solar zenith angle, μ_0 , for mean effective sizes of 50 and 75 μm

about 70, 55, 44 and 30% are shown for D_e of 25, 50, 75 and 100 μm , respectively. For solar absorptance, small ice crystals also absorb more solar radiation for IWPs up to 75 g m^{-2} . However, absorption of solar radiation also depends on forward scattering of cloud particles. Larger particles would have stronger forward scattering and absorb more solar radiation when the IWP is larger than about 75 g m^{-2} . The IR emissivity is significantly dependent on both D_e and IWP. For a given IWP of 20 g m^{-2} , emissivity differs by as much as 40% for D_e of 25 and 100 μm .

The effects of the ice crystal mean effective size on net radiative heating are illustrated in Fig. 3. In the calculations, we use an IWP of 26 g m^{-2} , which corresponds to an IWC of 0.013 g m^{-3} for a typical cirrostratus with a thickness of 2 km. This cloud is inserted in the standard atmospheric temperature and humidity profiles. A solar constant of 1365 W m^{-2} and a surface albedo of 0.1 are used in the solar radiation calculation. The optical depths for D_e of 50 and 75 μm are approximately 2 and 1, respectively. Net radiative heating rates that correspond to four cosines of the solar zenith angle of 0, 0.167, 0.5 and 0.833 are displayed in Fig. 3. When $\mu_0 = 0$, only IR heating/cooling takes place. In this case, a smaller D_e of 50 μm produces heating/cooling rates of about 0.6–0.7 $^{\circ}\text{C h}^{-1}$ close to the bottom and top of the cloud layer. For a D_e of 75 μm , the heating/cooling rates at the cloud bottom and top reduce by as much as a factor of two. This reduction is due to the fact that a cloud

having smaller D_e s emits more IR radiation at the colder cloud top. The cloud absorbs, at the same time, more IR radiation emitted from the warmer surface and atmosphere below, resulting in strong heating at the cloud base region. The solar heating rate increases with decreasing D_e and occurs primarily at the cloud top, where IR cooling is much more pronounced. For $\mu_0 = 0.833$, the solar heating rate is a factor of about three smaller than the IR cooling rate at the cloud top. It is evident from this illustration that the cloud field is largely controlled by IR heating/cooling and that the presence of small ice crystals may generate a steeper lapse rate within clouds.

4. The Role of the Mean Effective Cloud Particle Size in Large-Scale Cloud Processes

To investigate the sensitivity of cloud microphysics and radiative transfer parameterizations to large-scale cloud processes, the 3-D global cloud model developed by Lee et al. (1990) is used. This cloud model consists of thermodynamic equations for the prediction of water vapor, cloud liquid water content (LWC) and IWC, precipitation and temperature. However, the wind field is prescribed using the results from a general circulation model (GCM). The model has a 12-layer stretch vertical coordinate, which has a fine resolution in the lower levels. Cloud covers are computed from the threshold method. To compare with the observed cloud fields and to perform radiative transfer calcula-

tions, the model generated cloud parameters are strapped into low, middle and high clouds. The cloud microphysical processes considered in the model are evaporation, condensation, autoconversion, sublimation deposition, homogeneous nucleation, Bergeron processes, and gravitational settling for ice crystals. As described in Section 2, the gravitational settling is parameterized in terms of the bulk terminal velocity, which is critical to the simulation of IWC. Radiative transfer parameterizations for clouds follow those presented in Section 3. In particular, two cloud parameters, i.e., the mean effective size and IWP, are incorporated in radiation calculations. The analysis data for winds, temperature, and specific humidity at 12Z 1 July 1979 are used as initial values to perform the large-scale prediction for cloud fields.

We shall confine our discussion to the effects of the mean effective size of ice crystals on large-scale cloud simulations. The interactions and feedbacks of cloud microphysics, radiative transfer, and the cloud model are shown in Fig. 4. The model predicts IWC (and LWC), cloud cover, temperature, and specific humidity. The bulk terminal velocity and mean effective size are defined based on the cloud microphysics parameterizations. The IWC together with the model thickness give the IWP. The terminal velocity is directly related to IWC by means of parameterization and is interactive in the cloud model. Although we have developed a theoretical relationship between IWC and D_e , this relationship has yet to be verified. In this study, we shall treat D_e and IWP as two independent parameters to investigate the sensitivity

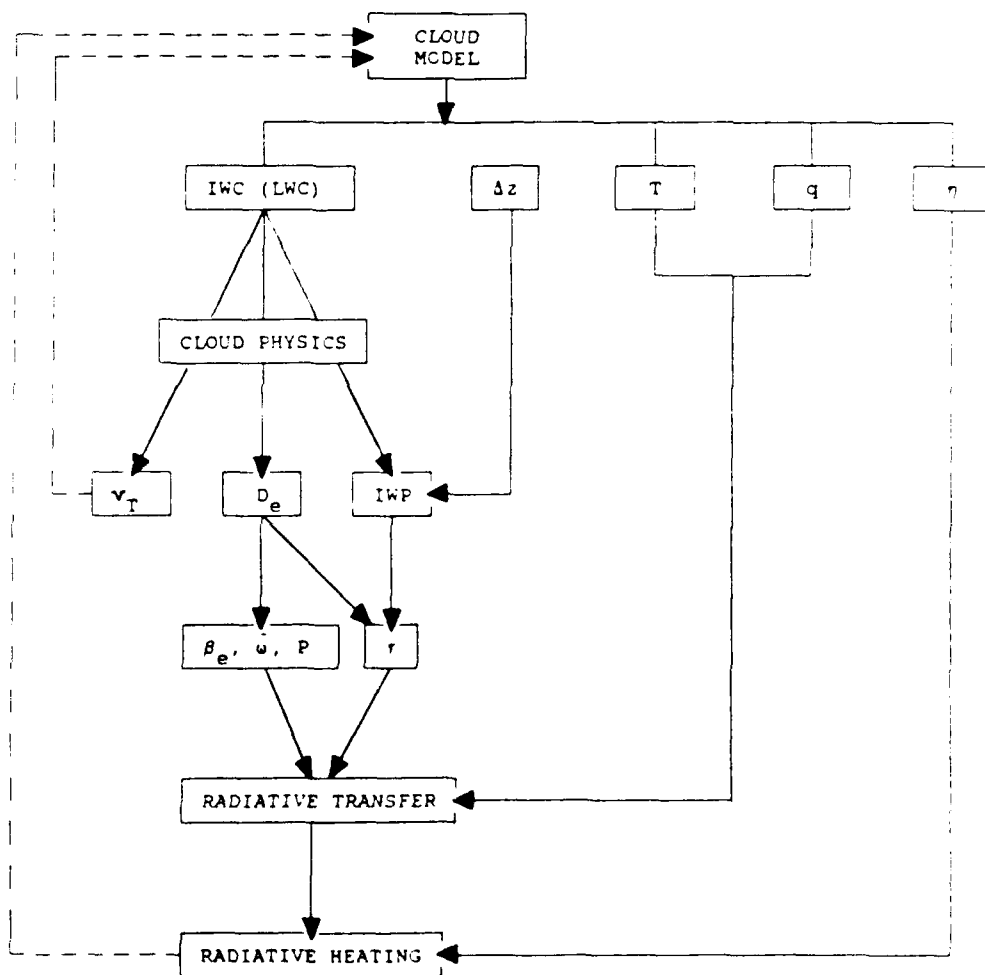


Fig. 4. Interactions and feedbacks of cloud microphysics, radiative transfer and the cloud model. In this diagram, η denotes cloud cover, V_T is the bulk terminal velocity, D_e is the mean effective size, β_e is the extinction coefficient, ω is the single-scattering albedo, P is the phase function, τ is the optical depth, T is temperature and q is the specific humidity.

of D_e on the simulations of large-scale cloud fields. Light scattering and absorption calculations for cloud particles require only information on particle size distribution, which is parameterized in terms of D_e . For radiative transfer calculations, the optical depth value is also needed. As shown in the preceding sections, the optical depth can be expressed in terms of D_e and IWP. Temperature and humidity are inputs in radiative transfer calculations. Lastly, cloud cover from the model is required to compute the average radiative heating in a model grid area. Radiative heating affects temperature directly via the thermodynamic heat equation, while the bulk terminal velocity affects IWC (and LWC) directly through the governing equations for IWC, LWC and precipitation.

Comparisons of the zonally averaged total cloud cover and outgoing longwave radiation (OLR) predicted from the model and derived from observations are shown in Figs. 5a and 5b. The

predicted cloud covers are averages of the results computed at 96 time steps over a 24 hour period. The observed cloud covers are taken from Henderson-Sellers (1986) based on the 3DNEPH data base for July 1979. It is well known that the 3DNEPH under- and over-estimates cloud cover in Arctic and Antarctic regions, respectively, for the summer season of the Northern Hemisphere. During this period, there are persistent stratus clouds over the Arctic region. However, the threshold method utilized in 3DNEPH has not been able to distinguish between the cold surface and clouds aloft. As a result, because of cold temperatures in the Antarctic region during the northern summer, the threshold technique overestimates cloud cover. The model underestimates cloud cover in the tropics because of the nature of the present 3-D global cloud model, which was developed primarily for stratiform clouds. It appears that improvements could be made if a cumulus convection program were added in the model. Nevertheless, there are general similarities between the predicted and observed cloud covers. The OLR fields computed from the model compare reasonably well with the monthly averaged data from ERB for July 1979. Discrepancies between the two may be explained by the cloud cover patterns described previously. In summary, the similarities between the model results and observations in terms of cloud cover and OLR are encouraging in view of the simplicity of the cloud model structure. Sensitivity experiments are carried out to investigate the relative importance of the mean effective size on the predicted large-scale cloud field.

The cloud model predicts IWC for high clouds and LWCs for middle and low clouds. Mean effective sizes of 50 and 75 μm are used in large-scale cloud simulations. The value of 50 μm corresponds to the mean effective size for a typical cirrostratus. Shown in Figs. 6a, 6b and 6c are the zonally averaged differences in the IR, solar and net heating rates predicted by the model for a 24 hour period. For smaller D_e , the IR emissivity is greater for high clouds, leading to more cooling at high cloud tops. However, the greater high cloud emissivity produces heating at high cloud bases and increases heating rates in the middle cloud level. The contour lines in Fig. 6a are for each $0.3^\circ\text{C day}^{-1}$. The increase of high cloud top cooling for smaller D_e is on the order of about

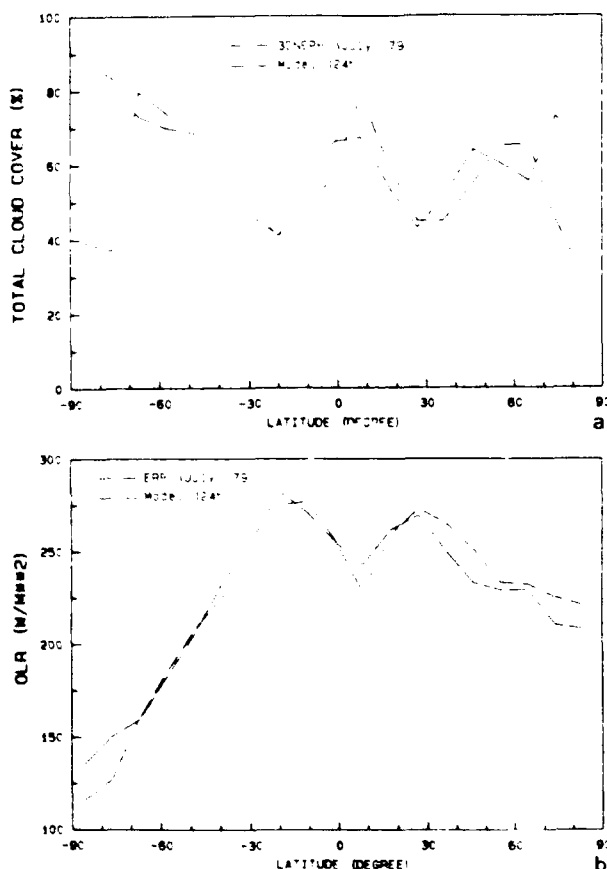


Fig. 5. Comparisons of the zonally averaged (a) total cloud cover and (b) OLR predicted from the model and derived from 3DNEPH and ERB for July 1979. The model results are for averages over a 24 h period.

$0.3^{\circ}\text{C day}^{-1}$ in cloud regions. In the middle cloud level, heating rates increase by about $0.6^{\circ}\text{C day}^{-1}$. These values are significant, since they are zonally averaged quantities. No change is seen in the heating rate patterns below middle clouds. The differences in solar heating rates produced by the two mean effective sizes are confined in the North-

ern Hemisphere because the July condition is used. A smaller D_e reflects more solar radiation and increases solar heating in high cloud top regions. At the same time, it reduces the solar fluxes available in the middle cloud level. The contour lines in Fig. 6b are for each $0.02^{\circ}\text{C day}^{-1}$, which is 15 times smaller than the IR heating/cooling rates. Figure 6c shows the net heating differences. The patterns are similar to the IR heating/cooling patterns. The exception is the reduction of cooling above high cloud top regions in the Northern Hemisphere.

Figures 7a–7c show the effects of the mean effective size on the simulation of temperature, cloud cover and IWC. Because of more cooling produced by a smaller D_e above the high cloud top, temperatures decrease there (Fig. 7a). The maximum decrease is on the order of about 0.2 – 0.4°C . However, temperature increases in the middle cloud level by about 0.4°C across the latitudes. In response to temperature decreases above the high cloud top, high cloud cover increases. The increase of high cloud cover is on the order of 4% across most latitudes (Fig. 7b). The use of different mean effective sizes of ice crystals significantly affects the calculation of middle cloud cover due to temperature increases. Except in the vicinity of 30°S where the occurrence of clouds is minimal, middle cloud cover is reduced by 3 to 4% between 60°N and 60°S latitudes because of warmer temperatures produced by IR heating. In terms of IWC for high clouds (Fig. 7c), differences produced by the two simulations are rather small because IWC is largely controlled by the bulk terminal velocity, which is interactive in the model. Variations in the mean effective size do not affect the bulk terminal velocity in the present experiments. It appears that IWC variations are primarily governed by microphysical processes. If the mean effective size could be made interactive through IWC, radiative perturbations would be important in the generation of IWC.

The preceding experiments have been carried out to explore the importance of the mean effective size of ice crystals in large-scale cloud simulations. Based on experimental results, small mean effective size, through radiative heating perturbations, would increase high cloud cover and, at the same time, reduce middle cloud cover. It is commonly recognized that the prime importance of high clouds is the downward emission of IR radiation

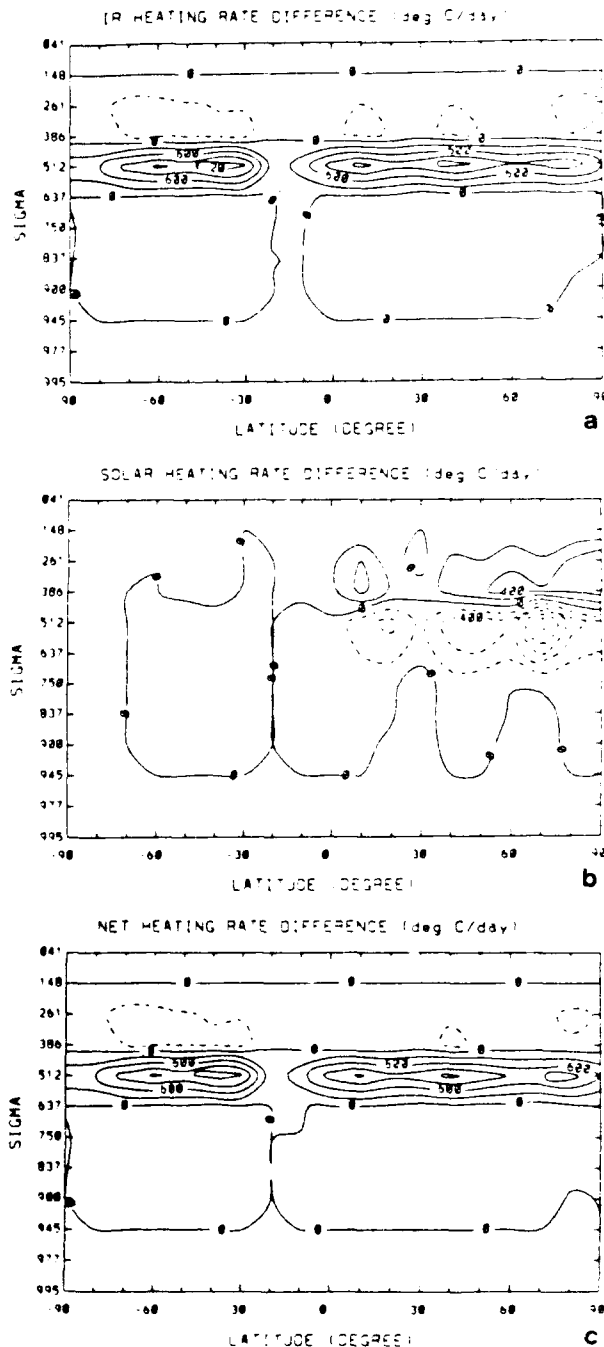


Fig. 6. Zonally averaged differences in (a) IR, (b) solar and (c) net heating rates for a 24 h period using mean effective sizes of 50 and $75\text{ }\mu\text{m}$ in numerical experiments

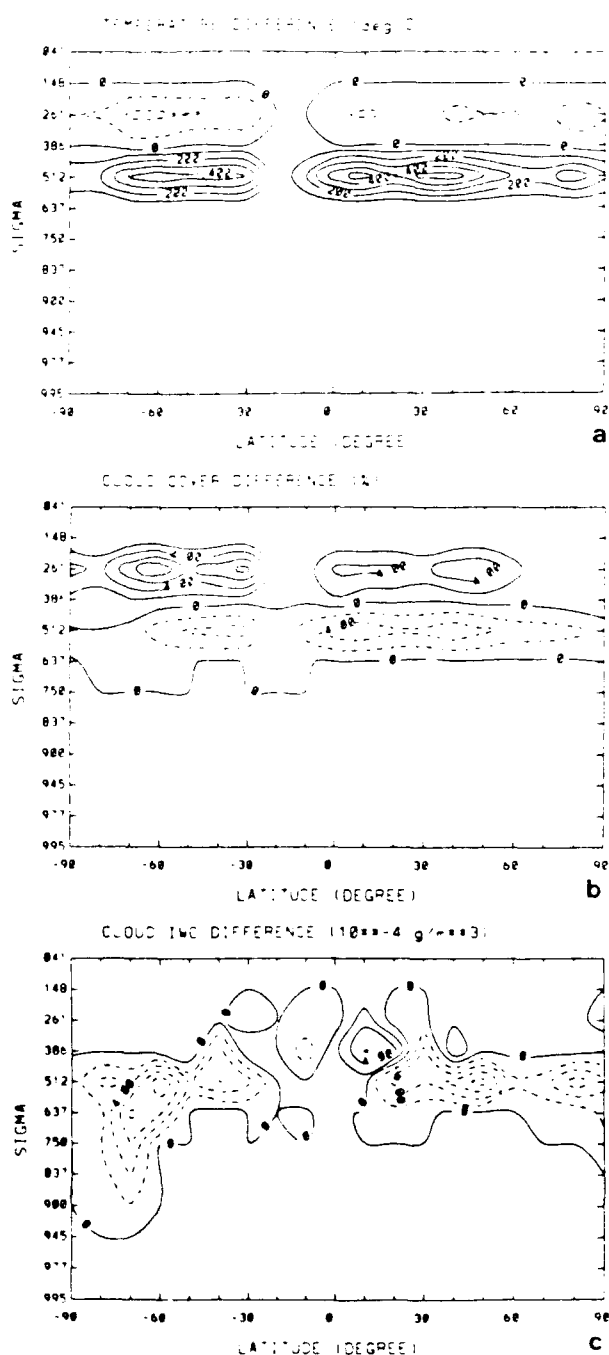


Fig. 7 Zonally averaged differences in (a) temperature, (b) cloud cover and (c) cloud IWC for a 24 h period using mean effective sizes of 50 and 75 μm in numerical experiments

(greenhouse effect). For middle clouds, it is the reflection of solar radiation (solar albedo effect). The increase of high cloud cover and the decrease of middle cloud cover would lead to the amplification of the greenhouse effect. Small mean effective sizes are normally considered to be signif-

icant in the reflection of sunlight. However, we have demonstrated in this study that the prevailing effects of small mean effective sizes are in the production of IR heating and cooling. The IR heating and cooling in the atmosphere produced by small mean effective sizes are much more significant than the solar heating counterpart.

5. Conclusions

Parameterization programs for cloud microphysics and radiative transfer involving ice clouds have been developed in conjunction with a 3-D global cloud model. We show that the mean effective size and IWP are two variables that are related to the optical depth. The mean effective size appears sufficient to define the ice crystal size distribution with respect to light scattering and absorption calculations. We illustrate the importance of the mean effective size in radiative transfer calculations in terms of solar reflectivity, IR emissivity and radiative heating. For a given IWP, smaller mean effective sizes reflect more solar radiation, emit more IR radiation and enhance net radiative heating cooling at the cloud top and bottom than larger sizes.

A 3-D global cloud model has been used to investigate the effects of the mean effective size of ice crystals on the simulation of cloud cover and IWC. This model has been verified through comparisons of the predicted cloud cover and OLR with monthly averaged values derived from 3DNEPH and ERB. High clouds that are composed of smaller mean effective sizes would produce more cooling at the cloud top and more heating at the cloud base, than high clouds composed of larger sizes. As a result of these heating/cooling patterns, more high cloud cover and less middle cloud cover are simulated from the model. Using the mean effective sizes of 50 and 75 μm , a $\sim 4\%$ increase and 3–4% decrease are shown for high and middle cloud covers, respectively. The radiative heating/cooling patterns, however, do not affect IWC for high clouds or LWC for middle clouds because the mean effective size is prescribed in the model. If a relationship could be established between the mean effective size and IWC, radiative heating through the mean effective size would influence the prediction of IWC as well as LWC for middle clouds.

On the basis of the preceding discussion, it would be important to develop a relationship between the mean effective size of ice crystals and IWC from aircraft experimental data. Second, radiative transfer parameterizations that encompass the mean effective size developed in Section 3 should be verified through concurrent radiation and cloud microphysics experiments involving ice clouds. Finally, the 3-D global cloud model may be improved by incorporating time varying wind fields to study their effects on the simulations of cloud parameters in the context of cloud microphysics radiative transfer parameterizations. The program may be accomplished by using a separate and parallel GCM to produce the required wind fields.

Acknowledgements

This research has been supported by the Air Force Office of Scientific Research Grant AFOSR87-0294, NSF Grant ATM88-15712 and NASA Grant NAG5-1050. We thank Professors H. Sundqvist and L. Donner for helpful comments on this paper.

References

- Asano, S., Sato, M., 1980: Light scattering by randomly oriented spheroidal particles. *Appl Opt.*, **19**, 962-974.
- Auer, A. H., Jr., Veal, D. L., 1970: The dimension of ice crystals in natural clouds. *J. Atmos. Sci.*, **29**, 919-926.
- Henderson-Sellers, A., 1986: Layered cloud amounts for January and July, 1979 from a 3-D Nephanalysis. *J. Climate Appl. Meteor.*, **25**, 118-132.
- Heymsfield, A. J., 1972: Ice crystal terminal velocities. *J. Atmos. Sci.*, **29**, 1348-1357.
- Heymsfield, A. J., 1977: Precipitation development in stratiform ice clouds: A microphysical and dynamical study. *J. Atmos. Sci.*, **34**, 367-381.
- Heymsfield, A. J., Platt, C. M. R., 1984: A parameterization of the particle size spectrum of ice clouds in terms of the ambient temperature and the ice water content. *J. Atmos. Sci.*, **41**, 846-856.
- Heymsfield, A. J., Donner, L. J., 1990: A scheme for parameterizing ice-cloud water content in general circulation models. *J. Atmos. Sci.*, **47**, 1865-1877.
- Hobbs, P. V., Chang, S., Locatelli, J. D., 1974: The dimensions and aggregation of ice particles in natural clouds. *J. Geophys. Res.*, **79**, 2199-2206.
- Jayaweera, K., Cottis, R. E., 1969: The fall velocities of plate-like and columnar ice crystals. *Quart. J. Roy. Meteor. Soc.*, **95**, 703-709.
- Lee, J. L., Ou, S. C., Liou, K. N., 1990: The effects of ice processes and infrared cooling on the formation of high clouds in a 3-D global cloud model. Preprint, *The Seventh Atmospheric Radiation Conference*, San Francisco, July 23-27, American Meteorological Society, Boston.
- Liou, K. N., Zheng, Q., 1984: A numerical experiment on the interactions of radiation clouds and dynamic processes in a general circulation model. *J. Atmos. Sci.*, **41**, 1513-1535.
- Liou, K. N., Fu, Q., Ackerman, T. P., 1988: A simple formulation of the delta-four-stream approximation for radiative transfer parameterizations. *J. Atmos. Sci.*, **45**, 1940-1947.
- Smith, R. N. B., 1990: A scheme for predicting layer clouds and their water content in a general circulation model. *Quart. J. Roy. Meteor. Soc.*, **116**, 435-460.
- Starr, D. C., Cox, S. K., 1985: Cirrus clouds. Part I: A cirrus cloud model. *J. Atmos. Sci.*, **42**, 2663-2694.
- Sundqvist, H., 1988: Parameterization of condensation and associated clouds in models for weather prediction and general circulation simulation. In: Schlesinger, M. E., (ed), *Physically-Based Modelling and Simulation of Climate and Climate Change*, Reidel, pp 433-451.
- Takano, Y., Liou, K. N., 1989a: Radiative transfer in cirrus clouds. I. Single-scattering and optical properties of hexagonal ice crystals. *J. Atmos. Sci.*, **46**, 3-19.
- Takano, Y., Liou, K. N., 1989b: Radiative transfer in cirrus clouds. II. Theory and computation of multiple scattering in an anisotropic medium. *J. Atmos. Sci.*, **46**, 20-36.

Authors' address: Prof. K. N. Liou, J. L. Lee, S. C. Ou, Q. Fu and Y. Takano, University of Utah, Department of Meteorology CARSS, Salt Lake City, Utah 84112, U.S.A.

INFRARED POLARIZATION SIGNATURE FROM CIRRUS CLOUDS

Y. Takano and K. N. Liou

Y. Takano and K. N. Liou are with the University of Utah, Department of Meteorology/Center for Atmospheric and Remote Sounding Studies, Salt Lake City, Utah 84112.

ABSTRACT

Maximum infrared polarization signature up to $\sim 1\%$ is predicted in tropical subvisual cirrus involving randomly oriented ice crystals based on radiative transfer calculations.

key words

cirrus infrared polarization

In the development of target detection based on infrared signature from space, the air and the ground, the effects of cirrus clouds, particularly subvisual cirrus, on infrared transmission must be understood. The radiative properties of cirrus clouds have been investigated by Takano and Liou^{1,2} using the scattering and absorption data derived from hexagonal ice crystals. In these papers, the radiative transfer method has been specifically developed for solar wavelengths in which thermal emission can be neglected. Liou et al.³ have extended the radiative transfer methodology to the thermal infrared wavelengths in order to study the transmission properties of thin cirrus clouds. In Takano and Liou¹, we have demonstrated that there are important polarization signatures of reflected sunlight from clouds. These signatures could be utilized to differentiate between spherical and nonspherical particles, as well as to distinguish among various nonspherical particles.

However, the information content of the polarization from cirrus clouds in the thermal infrared wavelengths has not been explored. The contribution to sky polarization from hexagonal and oriented ice crystals could be significant. It is the objective of this note to present some results regarding the radiance and polarization patterns for the 10 μm wavelength in a number of cirrus cloudy atmospheres.

The single-scattering properties for randomly oriented hexagonal ice crystals in the infrared wavelengths have been computed using the program developed by Takano and Liou¹. Figure 1a shows the phase function for hexagonal ice crystals with an aspect ratio ($L/2a$) of 120/60 ($\mu\text{m}/\mu\text{m}$) at the 10 μm wavelength, where L is the length and $2a$ is the width of a hexagonal crystal. The complex refractive index of ice⁴ used in this computation is 1.1991-10.051. For comparison, the phase function for the area-equivalent Mie spheres is also

shown in this figure. The peaks on the ice crystal phase function at the scattering angles of 14° and 27° correspond, respectively, to inner and outer haloes, which are at different angles than the standard 22° and 46° haloes in the visible because of the differences in refractive indices. Ice crystals scatter more light in backward directions than spheres. Figure 1b shows the degree of linear polarization due to single scattering of hexagonal crystals and spheres. Generally, the degree of linear polarization for hexagonal crystals is smaller than that for ice spheres. Using the single-scattering and polarization data, computations of the transfer of polarized infrared radiation in cirrus cloudy atmospheres have been carried out. Under plane parallel conditions, radiance and polarization patterns are azimuthally independent. They are only functions of the optical depth and zenith angle. In the computations, the surface is assumed to emit unpolarized radiation isotropically.

We have used tropical, mid-latitude winter, and arctic winter *atmospheric* profiles in performing the radiance and polarization calculations. The cloud and surface temperatures for these profiles, which are of prime importance in infrared radiative transfer calculations, are listed in Table 1. The heights of cirrus clouds are also included in this table. We used a columnar ice crystal shape with an aspect ratio (length/diameter) of $120/60$ ($\mu\text{m}/\mu\text{m}$) whose single scattering properties at $10\ \mu\text{m}$ are shown in Fig. 1.

Figure 2a-d shows the upward radiances at the cloud top and the downward radiances at the cloud base. Limb darkening and limb brightening are evident in upward and downward patterns, respectively. These patterns can also be seen in the window radiances⁵. When the cloud optical depth is small ($\tau_c=1$), the upward radiance for zenith angles less than $\sim 60^\circ$ are close to those emitted from the surface. For zenith angles larger than $\sim 60^\circ$, the upward radiance is reduced due

to cloud absorption of the radiation emitted from the surface. However, the downward radiance is enhanced due to the combined effects of cloud emission and the cloud reflection of surface radiation. The upward radiances decrease with the increase of optical depth in any models, because cirrus clouds absorb the radiation emitted by the surface. In contrast, the downward radiances increase with the increase of optical depth in any models because of the emission of cirrus. When the cloud optical depth is large ($\tau_c=4$), the downward radiances for zenith angles less than $\sim 60^\circ$ are close to those emitted from the cloud. As shown in this figure, radiance patterns depend on the atmospheric temperature profile used in the calculation. For $\tau_c=1$, the upward radiances increase according to the surface temperature. Exceptions are for the tropical case involving zenith angles greater than about 70° because of the lower temperature of the tropical anvil. For optically thick clouds with $\tau_c=4$, the upward radiances are largely produced by the cloud-top emission. The downward radiances depend primarily on the cloud temperature.

The degree of linear polarization⁶ patterns corresponding to Fig. 2a-d is illustrated in Fig. 3a-d. Because of the differences in upward and downward radiances, the linear polarization patterns are also different at the cloud top and base. It is noted that there is a significant difference in linear polarization patterns between thermal infrared and solar wavelengths. The magnitude of linear polarization displayed in Fig. 3, that is generally less than 1%, is much smaller than that in the case of solar radiation (see Fig. 8 in Takano and Liou²). This is in view of the fact that the surface and a small volume of cloud are assumed to emit unpolarized thermal radiation isotropically. We shall consider the optically thin case ($\tau_c=1$) in Fig. 3a-b in which the effect of single-scattering events on polarization is most pronounced. In this case,

radiation emerged from the cloud top is dominated by the emission from the surface and largely unpolarized for zenith angles less than 60° . For larger zenith angles, positive polarization may be produced by single scattering of the emitted unpolarized radiation from the surface as illustrated in Fig. 1b. At the cloud base, positive linear polarization is produced also due to the single scattering of the emitted unpolarized radiation from the surface. When τ_c is $1/8$, downward polarization can reach more than 1% at $\theta \approx 60^\circ$. When the cloud optical depth increases, polarization that is produced by single scattering is generally reduced. However, total polarization does not monotonically depend on optical depth, because of the combined effect of radiances from the cloud and the surface.

From Fig. 3a and c, it can be generally concluded that the upward polarization at the top of clouds composed of randomly oriented ice crystals is small, and for all practical purposes, the polarization can be neglected. In the case of downward components, polarization emerged from the tropical cirrus is greater than that emerged from the midlatitude and arctic cirrus by about one order of magnitude as shown in Fig. 3b and d. This feature can be explained as follows: First, consider only a cirrus cloud without an underlying surface. The degree of linear polarization at cloud boundaries is slightly negative and independent of the cloud temperature. This is because the effect of cloud temperature is canceled out in the denominator and numerator of $-Q/I$. Second, we add a surface below a thin cirrus. The total polarization is largely affected by the single scattering of surface-emitted radiation by ice crystals. Generally, single-scattered radiation has positive linear polarization as pointed out previously. The temperature difference between the surface and the cloud in the case of tropical cirrus is greater than that for the midlatitude and arctic

cirrus. As a result, the tropical cirrus shows more intense positive polarization than the midlatitude and arctic cirrus. Downward polarization for water clouds will also be small due to smaller differences between surface and cloud temperatures.

Radiance and polarization patterns have also been calculated for ice plates with an aspect ratio of 20/20 ($\mu\text{m}/\mu\text{m}$). Computed results are close to those for ice columns with an aspect ratio of 120/60 ($\mu\text{m}/\mu\text{m}$). The radiance and degree of linear polarization at the cirrus cloud boundaries depend more significantly on the difference between the surface and cloud temperatures than on the cloud particle size and shape. Downward infrared polarization at the cloud base in the case of tropical cirrus can reach more than 1%, which is greater than that for the cases of midlatitude and arctic cirrus by about one order of magnitude. At the wavelength of 10 μm , optical depths of air molecules and aerosols are small. Thus, detection of the tropical subvisual cirrus may be possible by measuring downward polarization at zenith angles of 60°-70° from the surface. This possibility will be explored in our future research efforts. The effects of horizontal orientation of ice crystals and the associated anisotropic emission on infrared polarization are also subjects for further investigation.

Acknowledgments. This work has been supported by the Office of Naval Technology through the Naval Air Development Center under contract N62269-89-C-0561. A part of the computations contained in this research work has been carried out on the San Diego supercomputer, CRAY Y-MP 8/864. We thank M. Hess for helpful comments on this note.

REFERENCES

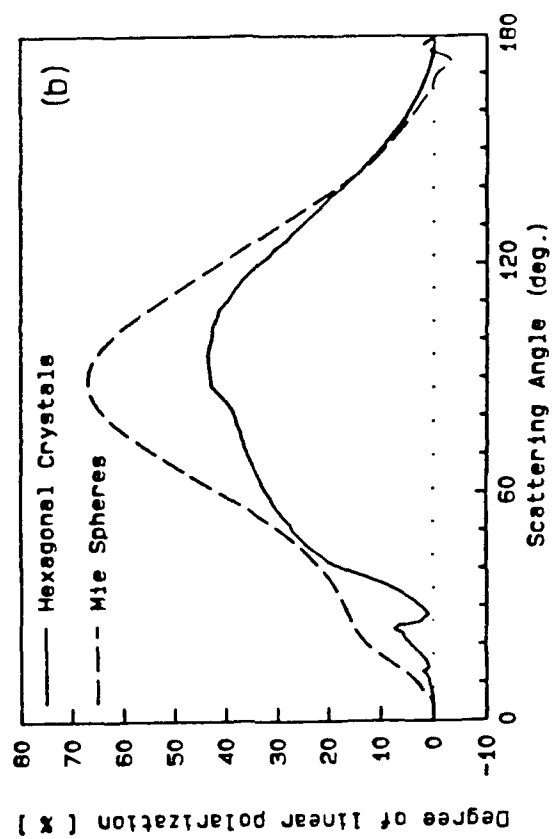
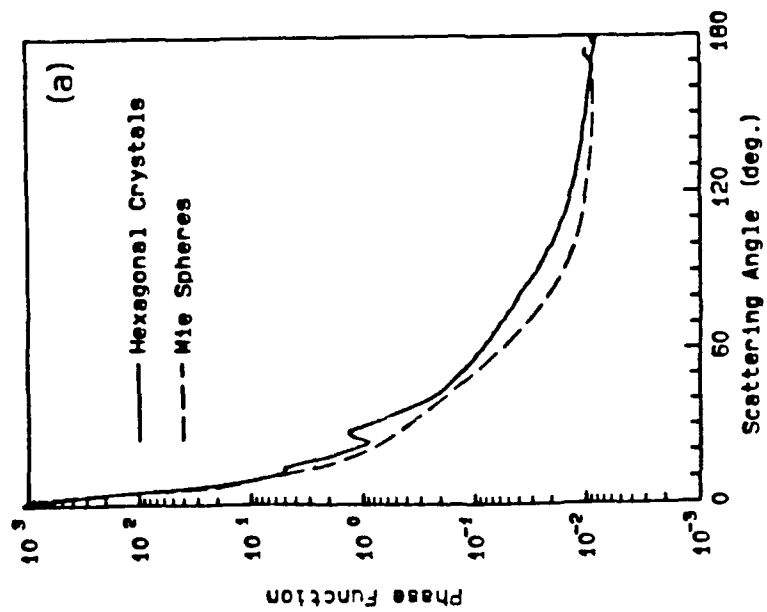
1. Y. Takano and K. N. Liou, "Solar radiative transfer in cirrus cloud. Part I: Single-scattering and optical properties of hexagonal ice crystals," J. Atmos. Sci., 46, 3-19 (1989).
2. Y. Takano and K. N. Liou, "Solar radiative transfer in cirrus clouds. Part II. Theory and computation of multiple scattering in an anisotropic medium," J. Atmos. Sci., 46, 20-36 (1989).
3. K. N. Liou, Y. Takano, S. C. Ou, A. J. Heymsfield, and W. Kreiss, "Infrared transmission through cirrus clouds: A radiative model for target detection," Appl. Opt., 29, 1886-1896 (1990).
4. S. Warren, "Optical constants of ice from the ultraviolet to the microwave," Appl. Opt., 23, 1206-1225 (1984).
5. K. N. Liou, "On the radiative properties of cirrus in the window region and their influence on remote sensing of the atmosphere," J. Atmos. Sci., 31, 522-532 (1974).
6. K. N. Liou, An Introduction to Atmospheric Radiation, (Academic Press, New York, 1980), Chap. 3, p. 81.

Figure Captions

- Fig. 1 (a) Scattering phase function and (b) degree of linear polarization for randomly oriented hexagonal ice crystals of $L/2a = 120/60$ ($\mu\text{m}/\mu\text{m}$) and the area equivalent Mie spheres at $\lambda = 10 \mu\text{m}$.
- Fig. 2 Radiances as a function of zenith/nadir angles on the boundaries of cirrus clouds in the three atmospheric profiles in the cases of (a) and (b) $\tau_c=1$ and (c) and (d) $\tau_c=4$.
- Fig. 3 Degree of linear polarization as a function of zenith/nadir angles on the boundaries of cirrus clouds in the three atmospheric profiles in the cases of (a) and (b) $\tau_c=1$ and (c) and (d) $\tau_c=4$.

Table 1. Cloud and surface temperature and cloud heights for three atmospheric profiles.

Profile	Cloud Height (km)	Cloud Temperature, T_c (K)	Surface Temperature, T_s (K)
Tropical	-15.0	200	300
Midlatitude Winter	-8.0	230	272
Arctic Winter	-6.5	227	257



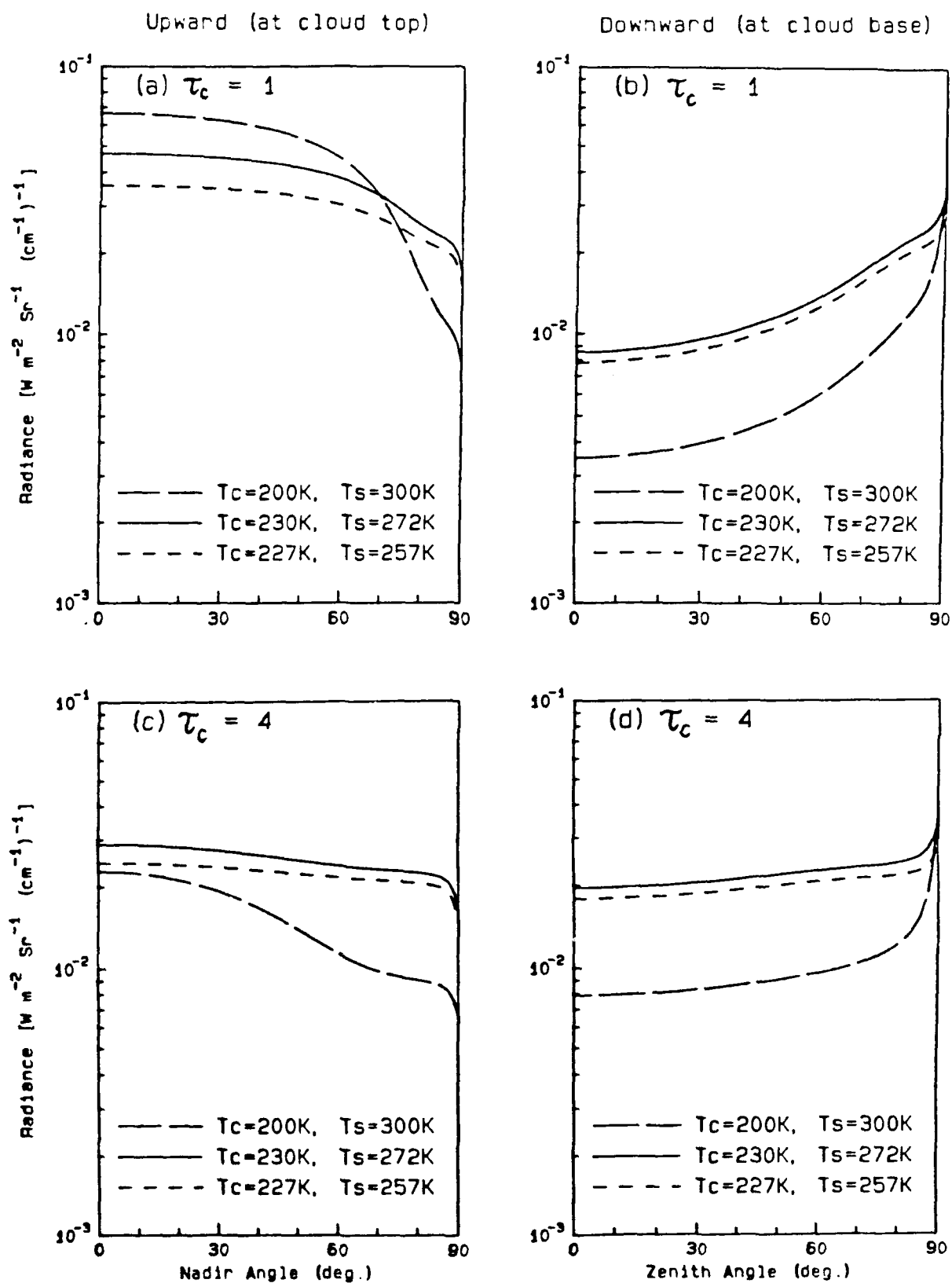
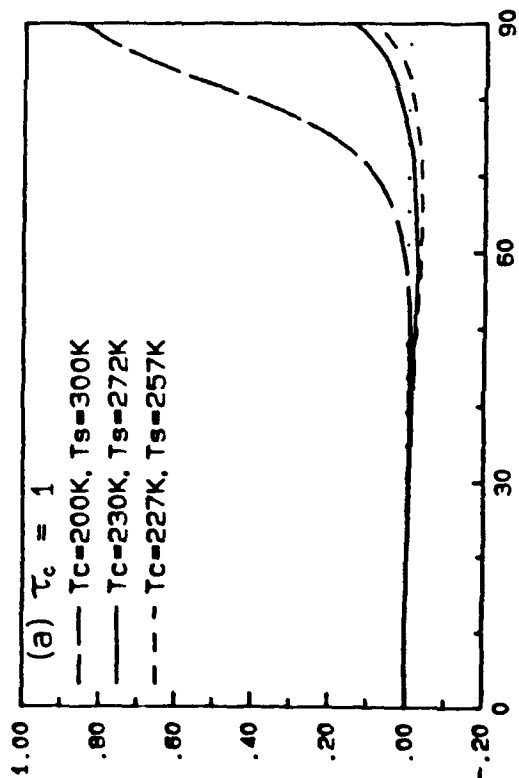
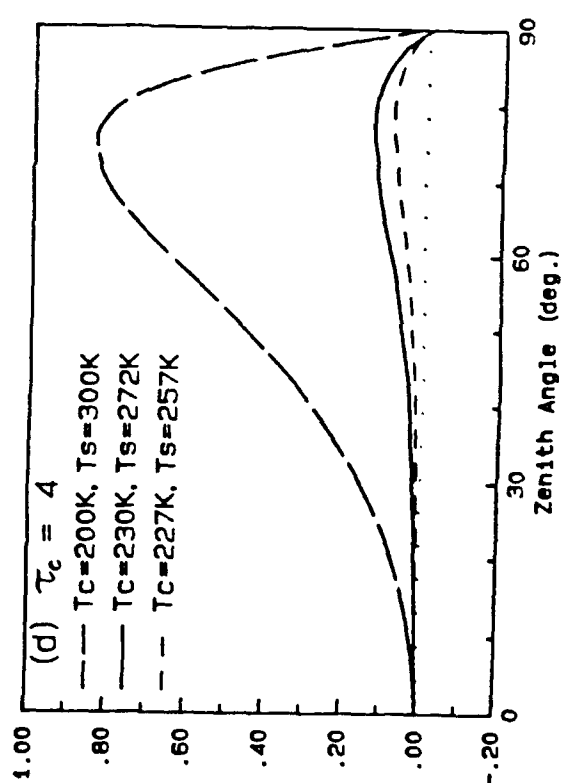
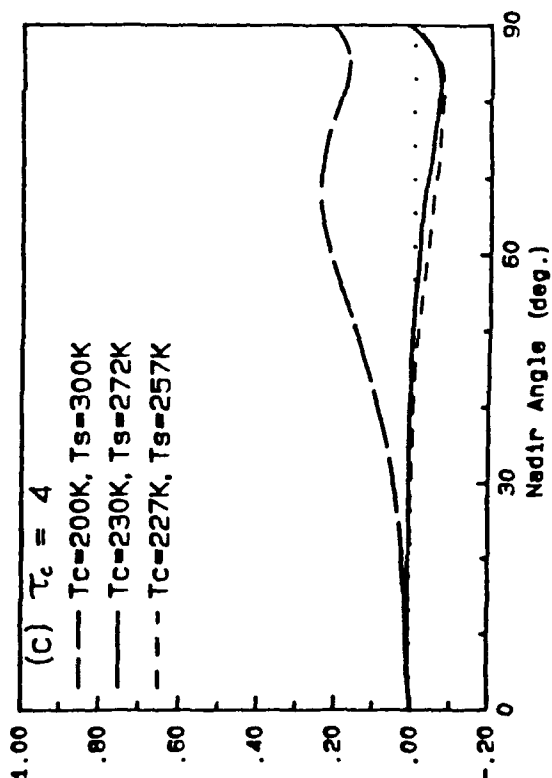
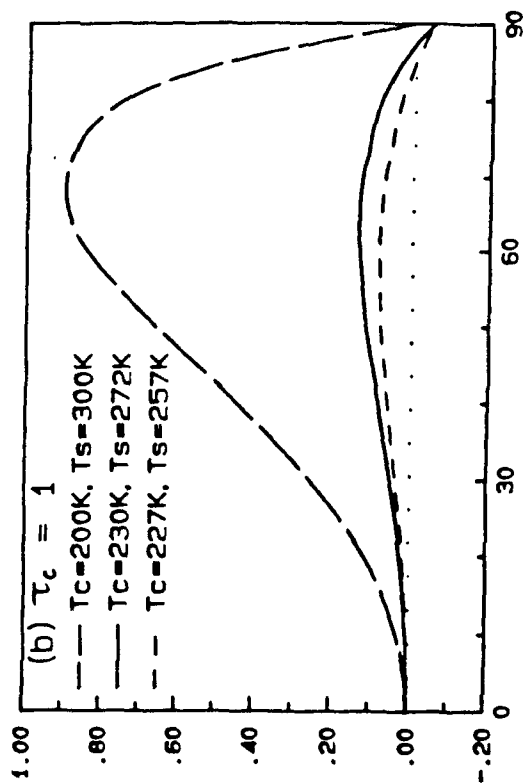


Fig. 2

Upward (at cloud top)



Downward (at cloud base)



Degree of Linear Polarization, $-Q/I$ (%)